Geophysical Journal International

*Geophys. J. Int.* (2022) **230,** 1895–1910
Advance Access publication 2022 April 22
GJI Geodynamics and Tectonics

https://doi.org/10.1093/gji/ggac159

# Structural controls on coseismic rupture revealed by the 2020 $M_w$ 6.0 Jiashi earthquake (Kepingtag belt, SW Tian Shan, China)

Siyu Wang [1] Edwin Nissen,[1] Léa Pousse-Beltran,[1,2] Timothy J. Craig [3] Ruohong Jiao[1] and Eric A. Bergman[4]

[1]*School of Earth and Ocean Sciences, University of Victoria, Victoria, BC V8P 3E6, Canada. E-mail: siyuwang@uvic.ca*
[2]*Institute des Sciences de la Terre, Université Grenoble Alpes,* 38058 *Grenoble, France*
[3]*School of Earth and Environment, COMET, Institute of Geophysics and Tectonics, University of Leeds, Leeds LS2 9JT, UK*
[4]*Global Seismological Services, Golden, CO* 80401*, USA*

Accepted 2022 April 20. Received 2022 April 8; in original form 2021 September 6



## SUMMARY

The Kepingtag (Kalpin) fold-and-thrust belt of the southern Chinese Tian Shan is characterized by active shortening and intense seismic activity. Geological cross-sections and seismic reflection profiles suggest thin-skinned, northward-dipping thrust sheets detached in an Upper Cambrian décollement. The 2020 January 19 $M_w$ 6.0 Jiashi earthquake provides an opportunity to investigate how coseismic deformation is accommodated in this structural setting. Coseismic surface deformation resolved with Sentinel-1 Interferometric Synthetic Aperture Radar (InSAR) is centred on the back limb of the frontal Kepingtag anticline. Elastic dislocation modelling suggests that the causative fault is located at ∼7 km depth and dips ∼7° northward, consistent with the inferred position of the décollement. Our calibrated relocation of the main shock hypocentre is consistent with eastward, unilateral rupture of this fault. The narrow slip pattern (length ∼37 km but width only ∼9 km) implies that there is a strong structural or lithological control on the rupture extent, with updip slip propagation possibly halted by an abrupt change in dip angle where the Kepingtag thrust is inferred to branch off the décollement. A depth discrepancy between main shock slip constrained by InSAR and teleseismic waveform modelling (∼7 km) and well-relocated aftershocks (∼10–20 km) may suggest that faults within sediments above the décollement exhibit velocity-strengthening friction.

**Key words:** Radar interferometry; Asia; Waveform inversion; Earthquake source observations; Folds and folding; Intraplate processes.

## 1 INTRODUCTION

Late Cenozoic crustal deformation in central Asia is dominated by reverse and strike-slip faulting and folding within and around the margins of the Tian Shan mountains. Geodetic data indicate that ∼6–9 mm yr$^{-1}$ of the present-day shortening occurs across the Chinese Tian Shan between the northwestern Tarim Basin and southern Kyrgyzstan (Reigber *et al.* 2001; Wang *et al.* 2020). The Kepingtag (Kalpin) fold-and-thrust belt has developed along part of the southern margin of this range (Fig. 1). This actively deforming belt is one of the most earthquake-prone regions of the Tian Shan and of China. In recent years, this intense seismicity has attracted much interest in the deformation style, rate and other characteristics of the Kepingtag belt (Allen *et al.* 1999; Zhou & Xu 2000; Yang *et al.* 2002, 2006; Ran *et al.* 2006; Zhang *et al.* 2008). Furthermore, it is one of the few parts of Tian Shan where deformation can be seen stepping into the surrounding foreland, with emergent thrust sheets predominantly vergent towards the Tarim basin in the south. Therefore, the deformation of the Kepingtag belt can also inform how the mountain ranges of southern Tian Shan grow through time.

Fold-and-thrust belts pose distinct challenges for seismic hazard assessment since much of the active faulting is buried. This is exemplified by iconic earthquakes such as the 1978 $M_s$ 7.4 Tabas, Iran earthquake (Walker *et al.* 2003) and the 1987 $M_w$ 5.9 Whittier and 1994 $M_w$ 6.7 Northridge, California earthquakes (e.g. Davis *et al.* 1989; Jones *et al.* 1994), each characterized by shallow folding and blind faulting without accompanying surface rupture. There are many other examples of large earthquakes that ruptured faults that were not previously mapped, and where historical and instrumental records were too short to have revealed the associated seismic hazard beforehand. Furthermore, fold-and-thrust belts contain a wide range of fault structures including décollements and ramp-and-flat thrusts, and it is often not clear which of these host large earthquakes and which creep aseismically (e.g. Copley 2014; Ainscoe *et al.* 2017;

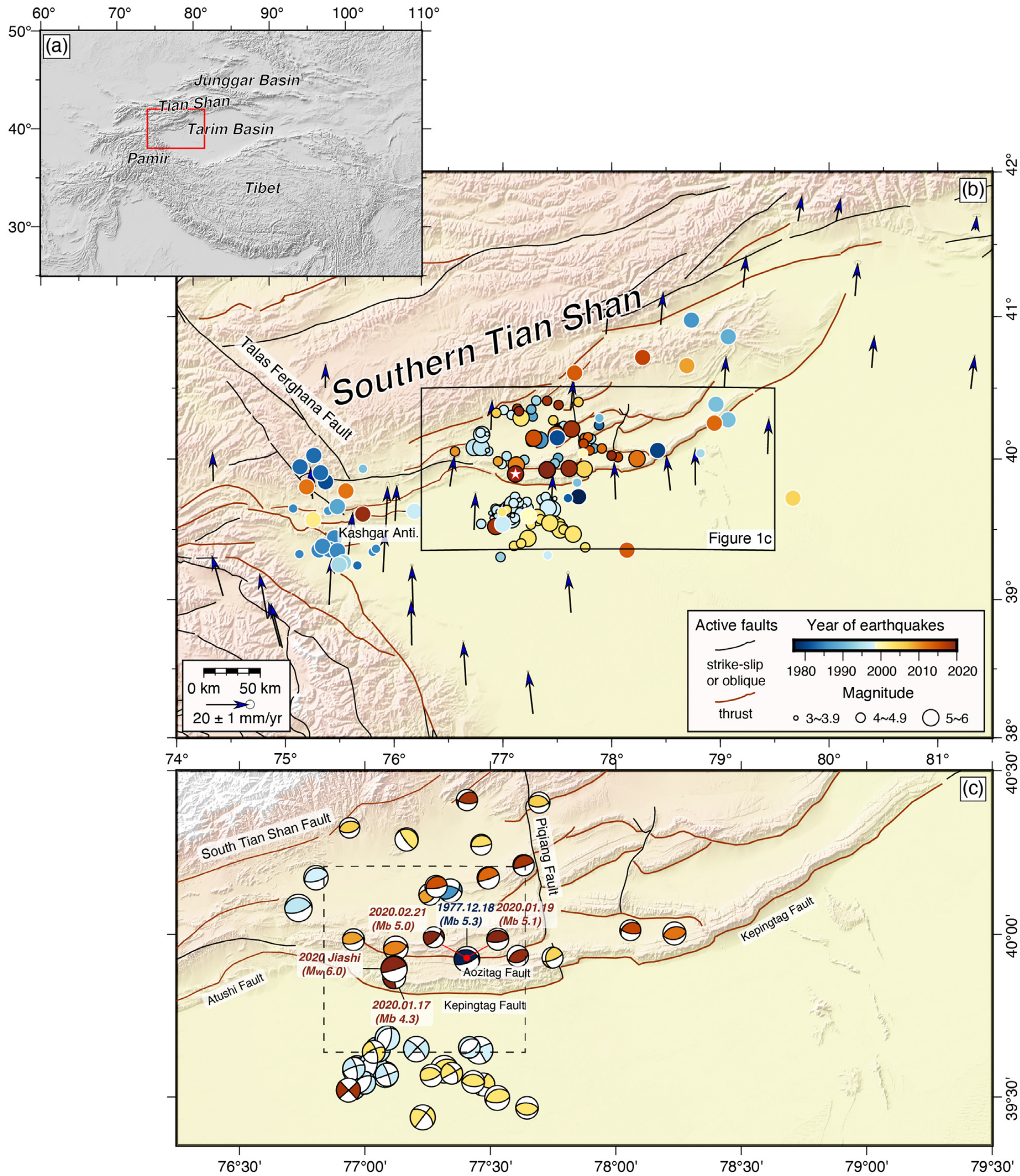


**Figure 1.** Tectonics and seismicity of the study area. (a) Shaded relief of the Himalayan orogeny with the location of panel (b) outlined in red. (b) Tectonic map of the southern Tian Shan. Instrumental seismicity is scaled by magnitude and coloured by year from 1977.12.18 to 2020.02.21. Our own relocated epicentres are shown with black outlines, while those from the United States Geological Survey (USGS) have white outlines. The white star is the relocated epicentre of the 2020 January 19 Jiashi main shock. Active faults are from the online database provided by the Institute of Geology, China Earthquake Administration (http://www.neotectonics.cn/arcgis/apps/webappviewer/index.html?id=3c0d8234c1dc43eaa0bec3ea03bb00bc) and Global Navigation Satellite Systems (GNSS) velocities relative to stable Eurasia are from Wang *et al.* (2020) with 95 per cent confidence ellipses. (c) Topography, active faults, and earthquakes of the Kepingtag fold-and-thrust belt. Focal mechanisms are from teleseismic body-waveform modelling studies or the Global Centroid Moment Tensor (CGMT) catalogue (see Table 1 for details) (Dziewonski 1981). They are plotted at our relocated epicentres, coloured by year and scaled by magnitude. The black dashed box shows the location of Fig. 2.

Mallick *et al.* 2021). It is also important to consider how subsurface structure and stratigraphy may influence rupture extents, and thus potential earthquake magnitudes (e.g. Elliott *et al.* 2011; Nissen *et al.* 2011).

On 2020 January 19 at 13:27:56 UTC, a $M_w$ 6.0 earthquake struck near Jiashi in the western Kepingtag belt (∼39.83°N, 77.21°E, Fig. 1), causing intense ground shaking and damage to hundreds of buildings. A regional seismic network recorded 1639 aftershocks as of 2020 February 11 (Ran *et al.* 2020), with the largest ($M_b$ 5.1) occurring ∼1 hr after the main shock. This sequence provides an opportunity to investigate patterns of seismicity and deformation in this region. Routine teleseismic moment tensor solutions for the main shock from the U.S. Geological Survey (USGS) and the Global Centroid Moment Tensor project (GCMT) implicate thrust or reverse faulting, but exhibit discrepancies of tens of degrees in strike, dip, and rake and of several kilometres in centroid depth and location. This makes it difficult to associate the earthquake with specific faulting or characterize its tectonic implications without further investigation (Engdahl *et al.* 2006; Weston *et al.* 2011; Wimpenny & Scott Watson 2020).

Interferometric Synthetic Aperture Radar (InSAR) observations and modelling can provide more precise constraints on fault geometries and depth extents of large, shallow continental earthquakes (e.g. Elliott *et al.* 2016). Furthermore, growing compilations of seismic phase arrival times can help relocate earthquake hypocentres more accurately which, in conjunction with InSAR slip models, can provide additional information on rupture directivity (e.g. Pousse-Beltran *et al.* 2020). In this paper, we map the surface deformation of the 2020 Jiashi earthquake using the Sentinel-1 InSAR imagery and characterize its subsurface fault geometry and slip distribution using elastic dislocation modelling. We provide an independent check on its mechanism and centroid depth using teleseismic body waveform modelling and pinpoint its hypocentre using a calibrated, multi-event relocation. We relate some striking features of the surface deformation and slip model to the subsurface structure of the Kepingtag belt. Our multi-event relocation also allows us to reassess earlier instrumental earthquakes in this region. These new results are used to re-evaluate the active tectonics and seismic hazard of the Kepingtag belt.

## 2 TECTONIC SETTING

The Tian Shan in Central Asia originally formed in the Palaeozoic, and most of the present topography of the mountain ranges resulted from Cenozoic reactivation as a result of the India-Eurasia collision (Windley *et al.* 1990; Hendrix *et al.* 1992; Avouac & Tapponnier 1993; Burchfiel *et al.* 1999). Over time, the deformation has propagated outward into the Tarim and Junggar basins, where along certain parts of the Tian Shan margins, intense folding and faulting have created sets of narrow ridges. The Kepingtag fold-and-thrust belt, located along the arid southern margin of the Chinese Tian Shan, offers one of the clearest examples of this basinward migration of active deformation (Fig. 1b).

### 2.1 Geology of the Kepingtag belt

About 200 km long by 50 km wide and trending WSW–ENE, the Kepingtag belt consists of fault-related folds associated with a series of south-verging, imbricated thrust stacks (Allen *et al.* 1999). Folded strata are composed of Cambrian–Ordovician Qiulitag group limestones, Middle Ordovician Saergan group limestone and dolomite, Silurian Kepingtag group sandstone, Devonian sandstone, Carboniferous Kangkelin group sandstone, lower Permian limestone and Palaeogene–Neogene Wuqia group sandstone and conglomerate (Chen *et al.* 2006; Yang *et al.* 2010). The thickness of the upper Palaeozoic strata in the Kepingtag belt increases from about 2 km in the south to greater than 4 km in the north (Yin *et al.* 1998). There is a major angular unconformity between the Palaeozoic strata and the Cenozoic foreland basin deposits, with the near absence of Mesozoic sedimentary rocks implying significant Palaeozoic crustal shortening.

The thick Palaeozoic sequence of mainly Upper Cambrian to Permian strata is exposed in a series of parallel anticlines (Xinjiang Bureau of Geology and Mineral Resources 1993). The hanging wall cut-offs of the imbricate thrusts have been eroded away. This thrust system is interpreted as thin-skinned, with fault-propagation folds detached in Upper Cambrian limestones along a décollement at ∼6–10 km depth according to seismic reflection profiles and balanced geological cross-sections (Nishidai & Berry 1990; Yin *et al.* 1998; Allen *et al.* 1999; Yang *et al.* 2010). The left-lateral Piqiang fault (Fig. 1) has developed perpendicular to the Kepingtag belt, dividing it into two (western and eastern) segments. Interpretations of satellite imagery and balanced cross-sections suggest that the thin-skinned imbricate thrusting and folding has accommodated crustal shortening strains of 20–28 per cent between the main Tian Shan and Tarim block, equivalent to ∼35 km across the western segment and ∼22 km across the eastern segment (Yin *et al.* 1998; Allen *et al.* 1999).

### 2.2 Seismicity of the Kepingtag belt and its foreland

Active crustal shortening and thickening of the southern Tian Shan is manifest in frequent reverse faulting earthquakes that cluster around the margins of the high topography with nodal planes oriented approximately parallel to the range (Ghose *et al.* 1998; Xu *et al.* 2006; Sloan *et al.* 2011). The Kepingtag belt and its adjacent foreland are amongst the most seismically active parts of the Tian Shan, with 36 earthquakes of $M_w$ 5.0–6.3 since the late 1970s (Fig. 1b and Table 1). The 1902 *Mw* 7.7 Atushi (Kashgar) earthquake, located ∼150 km west of our study area, hints that much larger earthquakes may be possible (Kulikova & Krüger 2017). Within the Kepingtag belt, instrumental seismicity is concentrated west of the Piqiang fault and the available focal mechanisms indicate a predominance of thrust and reverse faulting. Assuming that northward-dipping nodal planes represent faulting, dip angles range from ∼5°–60° with an average of around 30°. Only a few of these events have reliable centroid depths from detailed waveform modelling, mostly in the range 6–16 km, consistent with faulting within the lower sedimentary cover and the underlying basement (Fan *et al.* 1994; Ghose *et al.* 1998; Sloan *et al.* 2011). Sloan *et al.* (2011) placed a single outlier event at 34 km depth, within the middle-to-lower crust, but noted that its relatively complex waveforms could potentially be explained by a compound (multi-event) source mechanism at a much shallower depth.

Between 1997 and 1998, 13 earthquakes of $M_w$ 5.0–6.3 struck the foreland south of the Kepingtag belt. These included the destructive January–October 1997 Jiashi earthquake swarm, which caused 21 fatalities (Zhang *et al.* 1999). This sequence involved a mix of strike-slip and normal faulting with well-resolved centroid depths of ∼12–20 km (Sloan *et al.* 2011), as well as some smaller, deeper earthquakes located by a temporary regional network but without reliable focal mechanisms (Xu *et al.* 2006). The mechanisms and depths are challenging to interpret but may reflect flexural rebound of the Tarim basin under loading from the Tian Shan (Sloan *et al.* 2011). On 2003 February 24, the $M_w$ 6.2 Bachu–Jiashi earthquake struck the same area, resulting in 261 reported fatalities. In contrast with the 1997 swarm, the 2003 earthquake involved northward-dipping thrust faulting with a much shallower centroid depth of ∼5–7 km, interpreted to represent southward propagation of the Kepingtag belt into the Tarim basin (Sloan *et al.* 2011). It also produced an abundant aftershock sequence that was apparently concentrated in the middle crust between ∼15 and 25 km (Huang *et al.* 2006). Following the 2003 Bachu-Jiashi sequence, the Kepingtag belt and its foreland entered a relatively quiescent period of seismic activity, with no earthquake of magnitude 6 or above until the 2020 January 19 event.

**Table 1.** Earthquake source parameters in the Kepingtag belt and its foreland. Relocated hypocentres are from this study. The focal depth (FD) is followed by a superscript letter describing how it was calibrated: $d$ = teleseismic depth phases, $l$ = local-distance readings, $n$ = near-source station readings and $c$ = cluster default depths. Focal mechanisms are taken from (1) Fan *et al.* (1994), (2) Sloan *et al.* (2011), (3) Ghose *et al.* (1998), (4) the Global Centroid Moment Tensor (GCMT) catalogue and (5) this study. The centroid depth (CD) is also given a superscript letter that describes whether it was obtained by modelling ($t$) teleseismic body-waveforms, ($d$) teleseismic depth phases, ($r$) regional waveforms or ($i$) = InSAR surface displacements. Where only a less reliable GCMT centroid depth is available, we mark the solution with an asterisk.

| | | Relocated hypocentre | | | | Focal mechanism | | | | |
|---|---|---|---|---|---|---|---|---|---|---|
| Date | Time | Long. | Lat. | FD (km) | CD (km) | Strike | Dip | Rake | $M_w$ | Ref. |
| 1977.12.18 | 16:47 | 77.4065 | 39.9236 | $22^d$ | $7^t$ | 74 | 51 | 79 | 5.8 | *1* |
| 1986.04.25 | 16:12 | 77.3404 | 40.1340 | $13^d$ | 15* | 283 | 60 | 125 | 5.4 | *4* |
| 1996.03.19 | 15:00 | 76.7353 | 40.0810 | $13^l$ | $34^t$ | 234 | 16 | 87 | 6.0 | *2* |
| 1996.03.20 | 00:14 | 76.8644 | 40.0562 | $17^l$ | $6^r$ | 268 | 20 | 76 | 4.5 | *3* |
| 1996.03.22 | 08:26 | 76.7983 | 40.0816 | $15^l$ | $6^r$ | 260 | 18 | 78 | 5.2 | *3* |
| 1996.04.02 | 02:28 | 77.5587 | 40.2328 | $10^l$ | $16^r$ | 242 | 59 | 128 | 4.1 | *3* |
| 1997.01.21 | 01:48 | 77.2050 | 39.6475 | $11^l$ | $12^t$ | 317 | 85 | 177 | 5.4 | *2* |
| 1997.01.29 | 08:20 | 76.9678 | 39.5923 | $12^l$ | 33* | 04 | 83 | 132 | 5.2 | *4* |
| 1997.03.01 | 06:04 | 76.9532 | 39.5288 | $14^l$ | $14^d$ | 180 | 80 | −173 | 5.6 | *2,4* |
| 1997.04.05 | 23:36 | 76.9622 | 39.5832 | $12^l$ | $18^t$ | 177 | 64 | −139 | 5.4 | *2* |
| 1997.04.06 | 04:36 | 77.0809 | 39.5694 | $12^l$ | $17^t$ | 246 | 41 | −74 | 5.8 | *2* |
| 1997.04.06 | 12:58 | 77.0324 | 39.6105 | $17^l$ | $13^t$ | 210 | 38 | −74 | 5.1 | *2* |
| 1997.04.11 | 05:34 | 77.0326 | 39.6023 | $15^n$ | $20^t$ | 226 | 42 | −79 | 6.0 | *2* |
| 1997.04.12 | 21:09 | 77.0039 | 39.5334 | $14^n$ | $16^t$ | 239 | 27 | −74 | 5.1 | *2* |
| 1997.04.15 | 18:19 | 77.0506 | 39.6461 | $14^n$ | $18^t$ | 177 | 64 | −139 | 5.7 | *2* |
| 1997.06.24 | 09:24 | 76.9562 | 39.5877 | $16^n$ | 34* | 345 | 72 | −167 | 5.1 | *4* |
| 1997.10.17 | 17:35 | 77.0875 | 39.5686 | $25^d$ | 33* | 177 | 64 | −139 | 5.3 | *4* |
| 1998.03.19 | 13:51 | 76.8048 | 40.1732 | $15^l$ | $15^d$ | 243 | 5 | 79 | 5.6 | *2,4* |
| 1998.08.02 | 04:40 | 77.0897 | 39.6817 | $10^d$ | $15^t$ | 173 | 40 | −140 | 5.5 | *2* |
| 1998.08.03 | 15:15 | 77.0905 | 39.6527 | $15^l$ | $29^r$ | 253 | 10 | 129 | 4.6 | *2* |
| 1998.08.27 | 09:03 | 77.4554 | 39.6437 | $16^l$ | $15^t$ | 57 | 80 | 1 | 6.3 | *2* |
| 1998.09.03 | 06:43 | 77.4162 | 39.6528 | $25^d$ | $10^r$ | 179 | 59 | 178 | 4.8 | *2* |
| 1998.10.31 | 16:09 | 77.2469 | 39.6081 | $19^l$ | $14^r$ | 152 | 74 | −164 | 4.6 | *2* |
| 2003.01.04 | 11:07 | 77.0350 | 39.6389 | $14^l$ | 33* | 245 | 73 | −20 | 5.2 | *4* |
| 2003.02.24 | 02:03 | 77.3157 | 39.5852 | $19^l$ | $5^t$ | 280 | 17 | 115 | 6.2 | *2* |
| 2003.02.24 | 21:18 | 77.2653 | 39.5663 | $12^l$ | 15* | 289 | 33 | 126 | 5.2 | *4* |
| 2003.02.25 | 03:52 | 77.4717 | 39.5385 | $8^l$ | 15* | 239 | 33 | 62 | 5.3 | *4* |
| 2003.03.12 | 04:47 | 77.5273 | 39.4969 | $8^l$ | $7^d$ | 245 | 33 | 73 | 5.7 | *2,4* |
| 2003.03.15 | 22:59 | 77.3459 | 39.5733 | $9^l$ | 15* | 330 | 57 | 178 | 5.0 | *4* |
| 2003.03.30 | 23:15 | 77.4315 | 39.5462 | $17^l$ | $10^t$ | 287 | 27 | 117 | 5.2 | *2* |
| 2003.05.04 | 15:44 | 77.2305 | 39.4369 | $9^l$ | 15* | 308 | 53 | 179 | 5.8 | *4* |
| 2003.06.04 | 16:28 | 77.6458 | 39.4665 | $10^l$ | $10^d$ | 274 | 54 | 92 | 5.2 | *2,4* |
| 2003.09.26 | 23:35 | 77.1664 | 40.2902 | $30^d$ | 15* | 290 | 13 | 58 | 5.3 | *4* |
| 2004.10.07 | 16:14 | 77.4633 | 40.2740 | $12^l$ | 17* | 245 | 14 | 72 | 4.8 | *4* |
| 2005.03.24 | 07:37 | 77.7478 | 39.9288 | $11^d$ | 30* | 187 | 35 | 32 | 4.8 | *4* |
| 2006.06.08 | 11:34 | 77.6951 | 40.4025 | $6^d$ | 30* | 290 | 35 | 113 | 4.8 | *4* |
| 2006.09.06 | 07:51 | 76.9389 | 40.3257 | $15^l$ | 32* | 258 | 37 | 91 | 4.7 | *4* |
| 2009.04.22 | 09:26 | 77.2583 | 40.1229 | $11^d$ | 16* | 264 | 50 | 124 | 5.0 | *4* |
| 2009.10.16 | 02:56 | 76.9545 | 39.9836 | $15^d$ | 19* | 284 | 32 | 116 | 5.0 | *4* |
| 2011.08.11 | 10:06 | 77.1232 | 39.9575 | $19^d$ | 12* | 272 | 42 | 109 | 5.6 | *4* |
| 2012.08.11 | 09:34 | 78.2335 | 40.0027 | $15^d$ | 12* | 255 | 43 | 84 | 5.3 | *4* |
| 2013.03.11 | 03:01 | 77.4916 | 40.1729 | $9^d$ | 12* | 210 | 11 | 50 | 5.2 | *4* |
| 2015.01.10 | 06:50 | 77.2838 | 40.1469 | $14^c$ | 15* | 227 | 17 | 57 | 5.1 | *4* |
| 2016.07.09 | 16:36 | 78.0578 | 40.0128 | $14^c$ | 12* | 240 | 32 | 53 | 4.8 | *4* |
| 2018.04.12 | 10:41 | 77.4068 | 40.4104 | $17^l$ | 22* | 231 | 36 | 50 | 4.9 | *4* |
| 2018.09.03 | 21:52 | 76.9341 | 39.5211 | $14^c$ | 15* | 317 | 89 | 178 | 5.5 | *4* |
| 2018.11.03 | 21:36 | 77.6323 | 40.2120 | $14^c$ | 12* | 225 | 12 | 63 | 4.9 | *4* |
| 2019.01.06 | 16:22 | 77.6093 | 39.9331 | $6^d$ | 12* | 238 | 50 | 79 | 4.9 | *4* |
| 2020.01.17 | 16:05 | 77.1167 | 39.8682 | $12^d$ | 21* | 261 | 86 | −178 | 5.3 | *4* |
| 2020.01.19 | 13:27 | 77.1161 | 39.8944 | $11^d$ | $7^i$ | 279 | 7 | 115 | 6.0 | *5* |
| 2020.01.19 | 14:23 | 77.4089 | 39.9236 | $14^c$ | 18* | 268 | 22 | 95 | 5.1 | *4* |
| 2020.02.21 | 15:39 | 77.4059 | 39.9232 | $14^c$ | 14* | 287 | 46 | 143 | 4.8 | *4* |

The 2020 Jiashi sequence occurred within the frontal, western Kepingtag belt. The sequence was recorded by 13 permanent stations at ∼30–170 km distance and by two local stations ∼20 km SW and NW of the main shock epicentre, which were deployed by the Xinjiang Earthquake Administration 4 and 18 hr after the main shock, respectively. These regional recordings have been used as the basis of three previous seismological studies of the sequence, summarized below (Ran *et al.* 2020; Yao *et al.* 2021a; He *et al.*

2021). The $M_w$ 6.0 main shock was preceded by 2 d of foreshock activity involving ∼N–S-oriented left-lateral strike-slip faulting. The main shock itself ruptured an ∼E–W-oriented thrust or reverse fault, though there is disagreement amongst available seismological and geodetic models on its geometry and depth, which will be discussed further in light of our own results in Section 4. The main shock was followed by an energetic aftershock sequence of several hundred events that lasted at least 3 months. Double-difference relocated seismicity forms a 'T' shaped pattern in map view, with the main shock located at the bottom of the 'T' and aftershocks extending ∼20 km northward to the junction of the 'T' and from there, ∼20 km east and west for a total length of ∼40 km, with the greatest concentration of events along the western branch (Ran *et al.* 2020; He *et al.* 2021; Yao *et al.* 2021a). The double differencing also shows that the aftershocks are concentrated at depths of 10–20 km (Figs S12 and S13).

## 3 METHODS

### 3.1 InSAR measurements and modelling

We used InSAR to measure surface deformation in the 2020 January 19 earthquake, and elastic dislocation modelling to estimate the fault geometry and slip distribution. The raw data are from the European Space Agency's C-band Sentinel-1A satellite, with wavelength ∼5.6 cm. Two ascending tracks (056A and 129A) and one descending track (034D) capture the Jiashi main shock. Three, 12-d coseismic interferograms (11–23 January, 16–28 January and 10–22 January 2020) were processed using GAMMA software (Werner *et al.* 2000) and multilooked to four looks in range and 20 in azimuth to achieve a ∼30 m × 30 m pixel resolution. The topographic phase contribution was removed using the 30-m resolution Shuttle Radar Topographic Mission Digital Elevation Model, which was also used to geocode the interferograms. The two ascending-track interferograms were unwrapped using the branch-cut algorithm (Goldstein *et al.* 1988) while the noisier, descending-track interferogram was unwrapped using the Minimum Cost Flow algorithm.

The interferograms exhibit excellent coherence, reflecting the dry desert conditions and sparse vegetation of the southwestern Tian Shan. Coseismic surface deformation is easily distinguished in all three interferograms as a double fringe ellipse elongated in an E–W orientation (Figs 2a, d and g). The southern lobe is focused on the Kepingtag anticline and exhibits up to ∼7.5 cm of line-of-sight (LOS) displacement towards the satellite, and the northern lobe is centred along the Aozitag anticline and contains up to ∼5 cm of displacement away from the satellite (Figs 7a–c). The similarity of the fringe patterns in ascending and descending interferograms implies that the largest contribution to the observed LOS deformation is from uplift/subsidence rather than E–W lateral displacement, consistent with predominantly dip-slip faulting. We also observe some localized deformation along the southern Kepingtag range-front its proximal foreland basin. The short wavelengths, and absence of shallow aftershocks in this area, hints that this deformation is caused by secondary effects such as landsliding or liquefaction, and/or subsidence from agricultural activity (e.g. through aquifer drawdown).

After downsampling the LOS displacements using a quadtree algorithm to concentrate sampling in regions with high phase variance (Jónsson *et al.* 2002), we used a routine, two-step inversion strategy to estimate the causative fault parameters (e.g. Wright *et al.* 1999, 2004; Funning *et al.* 2005; Elliott *et al.* 2013, 2015; Ainscoe *et al.* 2017; Pousse-Beltran *et al.* 2020). In the first step, we inverted the downsampled data to solve for the optimal strike, dip, rake, slip, length and top and bottom depths of a rectangular, uniform slip model fault plane buried within an elastic half-space; we also jointly solved for nuisance parameters (a static shift and linear ramp in LOS displacement for each interferogram to account for their different unwrapping reference points, satellite orbital errors, and long-wavelength lateral variations in tropospheric delay) and weighted the single descending interferogram equal to the two ascending interferograms. We used Okada's expressions (Okada 1985) to relate model fault slip to deformation of the free surface, applied a non-linear, downhill Powell's algorithm (Press *et al.* 1992) to obtain the minimum misfit parameters, and ran 500 Monte Carlo restarts with random starting parameters to sample the parameter space fully and avoid local minima (Wright *et al.* 1999). Without firm constraints on how rheological properties vary with depth locally, we assumed an elastic half-space with standard Lamé parameters ($\lambda$ and $\mu$) of $3.2 \times 10^{10}$ Pa. We anticipate that this assumption only moderately impacts the retrieved fault parameters; for example, tests of layered and half-space elastic structures for a similar magnitude, buried earthquake in Tibet showed differences of $<1^\circ$ in fault strike and dip, $\sim6^\circ$ in rake, 0.2–0.5 km in fault length, top and bottom depths and centre coordinates, and 5–8 per cent in slip and moment (Bie *et al.* 2014). We also assumed a flat free surface, which is appropriate given the limited ($<1$ km) relief across the study area and is not expected to impact the retrieved fault parameters significantly (Li & Barnhart 2020). Finding a trade-off between slip and fault width—which is common for buried earthquakes (e.g. Funning *et al.* 2005; Elliott *et al.* 2013)—we obtained the initial fault geometry by fixing slip to 1.0 m. Inversions performed with 0.5, 1.5 and 2.0 m show that this choice makes no significant difference to the resulting fault geometry, with variations of $<1^\circ$ in the resulting model fault strike, dip and rake and $<0.5$ km in fault length and fault centre point latitude, longitude and depth (Table S1).

In the second step, we estimated the slip distribution by extending the uniform slip model fault plane along strike and up- and downdip, dividing it into 1 km × 1 km subfault patches, and solving for slip on each patch (with rake fixed to the uniform slip solution) using a Laplacian operator to vary smoothing (Wright *et al.* 2004; Funning *et al.* 2005) and a non-negative least squares algorithm to ensure positive slip (Bro & De Jong 1997). We solved for the best-fitting slip model and nuiscance parameters, m, using the equation,

$$\begin{pmatrix} \mathbf{G} \\ \kappa\nabla^2 \end{pmatrix} \mathbf{m} = \begin{pmatrix} \mathbf{d} \\ 0 \end{pmatrix},$$

where G is the matrix of Green's functions (LOS displacements calculated at downsampled data locations using the formulation of Okada (1985) for 1 m of slip on each fault patch), $\nabla^2$ is the finite difference approximation of the Laplacian operator which acts to smooth the distribution of slip, $\kappa$ is a scalar smoothing factor which determines the relative importance of the smoothing operator and $d$ contains the downsampled LOS displacements. We settled upon a preferred smoothing factor that represents a compromise between decreasing the fault slip roughness to prevent unrealistic, oscillating slip distributions, while minimizing the resulting increase in misfit (Wright *et al.* 2004). The resulting model still included a few outlier slip patches that lay several kilometres updip from the main slip distribution, which we consider spurious and exclude from our final, reported results. These are tabulated in Table S3, and were used to generate the forward model and residual interferograms shown in Fig. 2.

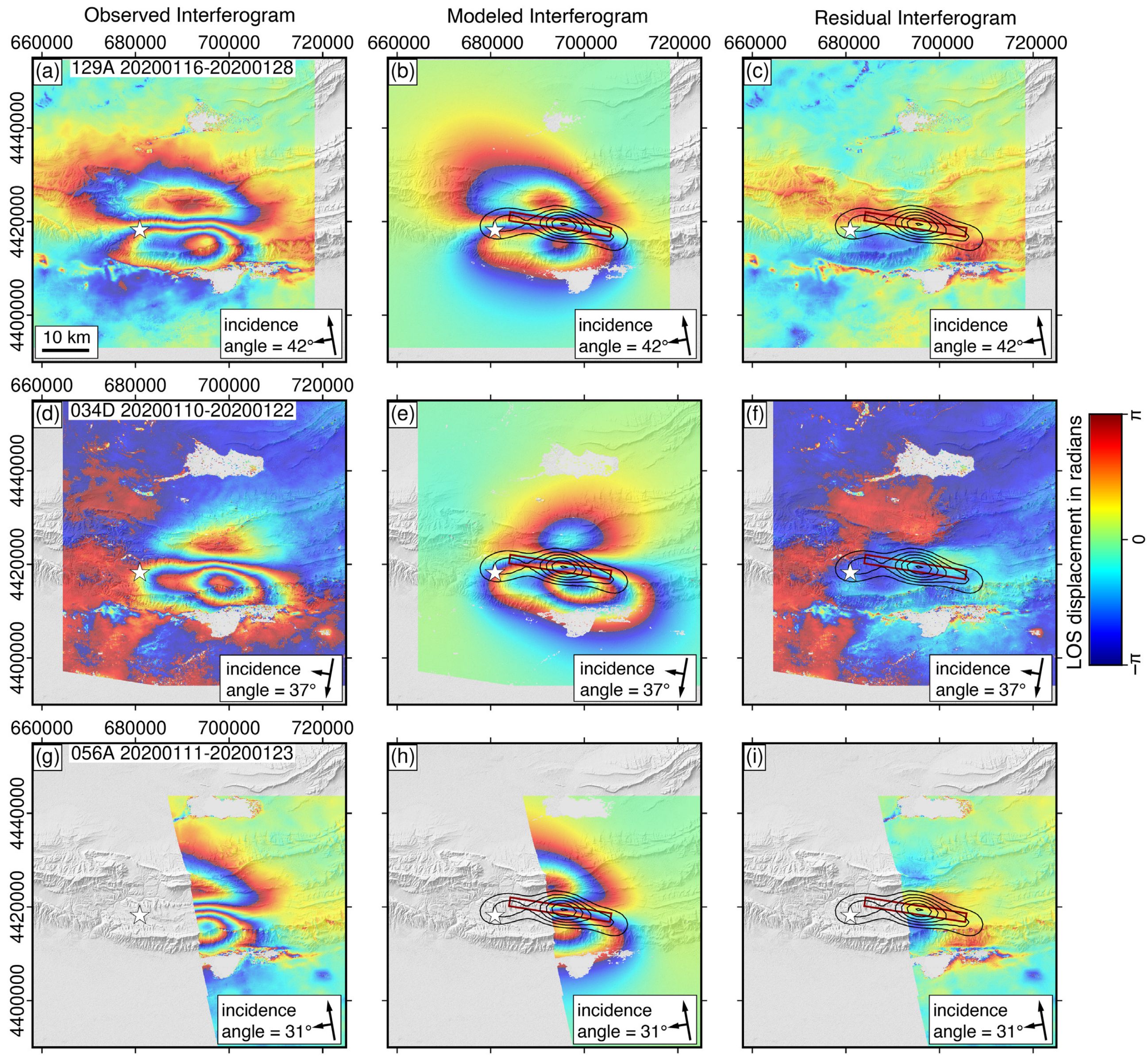


**Figure 2.** Left-hand column: observed, (centre) distributed slip model and (right) residual interferograms of the 2020 Jiashi main shock rupture. Modelling was performed using unwrapped LOS displacements, but here we plot the original, wrapped (filtered) interferograms since these show more clearly the shape of the deformation field. The coordinates are in UTM 43N. Colour cycles of blue through yellow to red indicate motion away from the satellite and one colour cycle ($2\pi$ radians) represents a half radar wavelength (2.8 cm) of LOS displacement. The satellite track azimuths and LOS direction with local angle of incidence are indicated by the longer and shorter black arrows, respectively. The white star indicates the relocated main shock epicentre. In the central and right-hand panels, 10 cm model slip contours are shown in black and the outline of the uniform slip model fault plane is marked in dark red.

Given the structural complexity of the Kepingtag belt, we also investigated whether the Jiashi earthquake may have involved non-planar rupture geometries by inverting the InSAR displacements for two uniform slip model fault planes (e.g. Pousse-Beltran *et al.* 2020). We explored a range of listric and antilistric configurations by matching the top depth of a deeper model fault to the bottom depth of a shallower model fault, and allowing their dips to vary independently and up to angles as steep as 32.5°. Though the large number of free parameters in these two-fault models make it challenging to explore fully this parameter space, none of the two-fault configurations that we tested produced a realistic geometry that improved upon the misfit of the simple, single-fault model. This leads us to favour involvement of a single, planar fault.

We did not have access to GNSS data that could potentially constrain our slip model further, though we know of six stations within ∼100 km of the main shock that may have exhibited coseismic offsets (Fig. 1; Wang *et al.* 2020). Instead, we provide a table of displacements at these sites predicted by our preferred, InSAR-derived distributed slip model (Table S6). These could be used for comparison by any future GNSS study of the Jiashi sequence.

### 3.2 Calibrated hypocentre relocations

We relocated hypocentres of the 2020 January 19 Jiashi main shock and its principal foreshock ($m_b$ 4.3) and two largest aftershocks ($m_b$

5.1 and 5.0) using teleseismic, regional and local seismic phase arrival times. Thirty-seven well-recorded background events starting from 2003 were also relocated, providing the repeated phase observations at common stations and the improved azimuthal coverage at local distances needed to calibrate the cluster, by which we mean minimizing hypocentral biases from unknown Earth structure and reliably quantifying their uncertainties (Benz 2021). We adopt the Hypocentroidal Decomposition relocation approach of Jordan & Sverdrup (1981) which separates the relocation into two distinct inverse problems, each reliant on customized phase arrival time data. We solve first for the relative locations of each hypocentre with respect to the reference hypocentroid (defined as the arithmetic mean of all individual event hypocentres within the cluster) using arrival data at all distances, allowing us to capitalize upon the abundance of teleseismic phase picks available for larger events in the cluster. We then solve for the absolute location of the hypocentroid using only locally recorded, direct *Pg* and *Sg* phases, which are impacted least by unknown Earth structure. This enables us to update the absolute hypocentre coordinates of every event in the cluster. In other, comparably instrumented regions, direct calibrations (ones that utilize local seismic data to solve for the hypocentroid) have resolved epicentres to within ∼1–2 km (at 90 per cent confidence) and focal depths to within ∼5 km (Karasözen *et al.* 2019), improving substantially on the uncertainties of routine catalogues such as the USGS and GCMT (Engdahl *et al.* 2006). Juxtaposing calibrated epicentres with InSAR-derived slip models can distinguish bilateral from unilateral rupture propagation (e.g. Gaudreau *et al.* 2019; Pousse-Beltran *et al.* 2020) and help resolve ambiguities in subsurface fault geometry, which are otherwise commonplace for buried earthquakes (e.g. Roustaei *et al.* 2010; Copley *et al.* 2015; Elliott *et al.* 2015; Karasözen *et al.* 2018).

The cluster was relocated and calibrated in the *Mloc* program (Walker *et al.* 2011; Karasözen *et al.* 2016; Benz 2021) using a customized traveltime model (Table S2) comprising a 3-layered crust of thickness 50 km—consistent with several previous estimates of regional Moho depths (Gao *et al.* 2013, and references therein)—over the upper mantle portion of the global 1-D model ak135 (Kennett *et al.* 1995). For the best-recorded events, we estimated focal depths using local arrival times; for others, we relied upon teleseismic depth phases or simply fixed the focal depth to a representative cluster default of 14 km (Fig. S1). We estimated the hypocentroid using epicentral distances of up to 2°, for which there is excellent azimuthal coverage (Fig. S2); average residual travel times for phases used in this direct calibration are 0.0 s for *Pg* and 0.1 s for *Sg* (Fig. S3). Observed phase arrivals and theoretical travel times for distances of up to 4°, 15° (for shear phases) and 30° are shown in Figs S4–S6. The final relocated hypocentres, including epicentral uncertainties at 90 per cent confidence, are provided in Table S3.

Our results were then combined with an earlier *Mloc* relocation cluster focused on the 1997 Jiashi earthquake swarm and the 2003 Bachu-Jiashi earthquake in the foreland south of the Kepingtag belt (Benz 2021). The earlier cluster adopted the same relocation procedure and the same regional velocity structure for the crust and upper mantle as this study. The earlier cluster is available through the Global Catalog of Calibrated Earthquake Locations (GCCEL) database (Benz 2021) and figures in the main paper incorporate both relocated data sets.

### 3.3 Teleseismic body waveform inversion

Finally, we used teleseismic body waveform modelling to provide additional constraints on the main shock source depth and mechanism, complementing those from InSAR analysis. Modelling of both seismological and geodetic data is important when there are disagreements in the depth of faulting, as is the case for the Jiashi earthquake (see Section 4). Centroid depths obtained from waveform modelling can also help clarify whether fault slip resolved by InSAR models occurred coseismically or through afterslip (Nissen *et al.* 2014).

We followed the approach of Heimann *et al.* (2018), and inverted vertical and transverse component data from stations between 3300 and 9900 km from the reported earthquake location (Fig. S7). Waveforms were filtered between 0.01 and 1 Hz, and we used a window starting 15 s before, and ending 25 s after, the principle phase (*P* for vertical component waveforms, *S* for transverse component waveforms). Synthetic seismograms were generated using the velocity structure determined in our calibrated relocation (Section 3.2 and Table S2). The source-time function is constrained to be a variable-duration half-sinusoid—appropriate for an earthquake of this size, and for the frequencies used in our inversions. Observed data and synthetics were aligned using cross correlation. The Bayesian approach outlined in Heimann *et al.* (2018) allows for the full sampling of the parameter space available in source depth, latitude, longitude, magnitude and mechanism (Figs S8–S9). Misfits between observed and synthetic waveforms are plotted in Figs S10–S11.

## 4 RESULTS

Our best-fitting InSAR uniform slip model fault strikes 279°, dips 7°N, has a slight right-lateral component (rake 115°), and is ∼22 km long by ∼2 km wide, centred at 7 km depth (Table 2). To further test model sensitivity to centroid depth, we ran the inversion by prescribing different (fixed) top and bottom depths while allowing other parameters to vary freely. We also undertook similar tests of model sensitivity to dipping angle and fault width (aspect ratio). There is a fairly steep increase in misfit at fault centre depths shallower or deeper than the minimum misfit value of 7 km (Fig. 3). For the equivalent dip sensitivity test, we find low misfits for dip angles of 5–10°, but abrupt increases in root mean square error outside of this range (Fig. 4a). For the fault width test, we find that extending the fault plane up- and downdip leads to larger misfits, particularly when the aspect ratio (length to width) is forced from the minimum misfit value of ∼12 to below ∼6. This shows that the highly-elongated model rupture area is real (Fig. 4b).

Compared to the uniform slip model, our preferred distributed slip model is longer at ∼37 km and wider at ∼9 km, but remains centred at ∼7 km depth (Fig. 5). The slip distribution is characteristically narrow, with an aspect ratio (length to width) of around 4. The peak slip is ∼0.5 m and the model moment is $\sim 1.75 \times 10^{18}$ N. The resultant forward model interferogram matches the observed surface deformation closely, with less than one residual fringe and a root mean square residual of ∼0.25 cm (Figs 2c, f and i), which is substantially lower than that of the uniform slip model (∼0.35 cm). The close agreement between observed and forward model coseismic fringe patterns implies that the more localized deformation along the Kepingtag rangefront had negligible impact on our modelling.

**Table 2.** Source parameters of the 2020 Jiashi main shock inferred from our model and other sources. The longitude and latitude listed for our InSAR-derived models (first two rows) represent the surface projection of the model slip plane; our relocated epicentre is 77.117°E and 39.894°N. The other InSAR studies parametrize the fault location differently. Depths are given as the top, middle (or centroid) and bottom depths of the slip plane in that order. L and W are length and width, respectively. Yu *et al.* (2020) prefer their listric, two fault model with a deeper, flatter segment fixed at 2° dip and a shallower, steeper ramp at 52°. Yao *et al.* (2021b) used uniform slip of 0.32 m in their InSAR-derived model, which may account for their much larger model fault plane.

| Source | Long. | Lat. | Strike | Dip | Rake | Depth (km) | L/W (km) | Moment (Nm) | $M_w$ |
|---|---|---|---|---|---|---|---|---|---|
| This study, uniform slip | 77.279° | 39.902° | 279° | 7° | 115° | 7.0/7.1/7.2 | 22/2 | $1.31 \times 10^{18}$ | 6.0 |
| This study, distributed slip | 77.165° | 39.416° | 279° | 7° | 115° | 6.3/7.0/7.6 | 37/9 | $1.75\times 10^{18}$ | 6.0 |
| USGS body-wave | 77.11° | 39.84° | 262° | 9° | 105° | –/4/– | – | $1.493 \times 10^{18}$ | 6.1 |
| USGS *W*-phase | 77.11° | 39.84° | 221° | 20° | 72° | –/19.5/– | – | $1.387 \times 10^{18}$ | 6.0 |
| CGMT | 77.19° | 39.80° | 196° | 38° | 31° | –/11/– | – | $1.39 \times 10^{18}$ | 6.0 |
| Yu *et al.* (2020), 1 fault | 77.30° | 39.91° | 275° | 9° | 111° | –/6.3/– | – | – | 6.1 |
| Yu *et al.* (2020), 2 faults | 77.30° | 39.90° | 275° | 2°/52° | 111° | –/4.15/– | – | – | 6.1 |
| Yao *et al.* (2021a) | 77.86° | 39.31° | 269° | 20° | 92° | 4/5/6 | 58/30 | $2.29 \times 10^{18}$ | 6.2 |
| He *et al.* (2021) | 77.45° | 39.79° | 276° | 10.2° | 109° | 5/7.3/9.6 | 50/26 | $– \times 10^{18}$ | 6.08 |

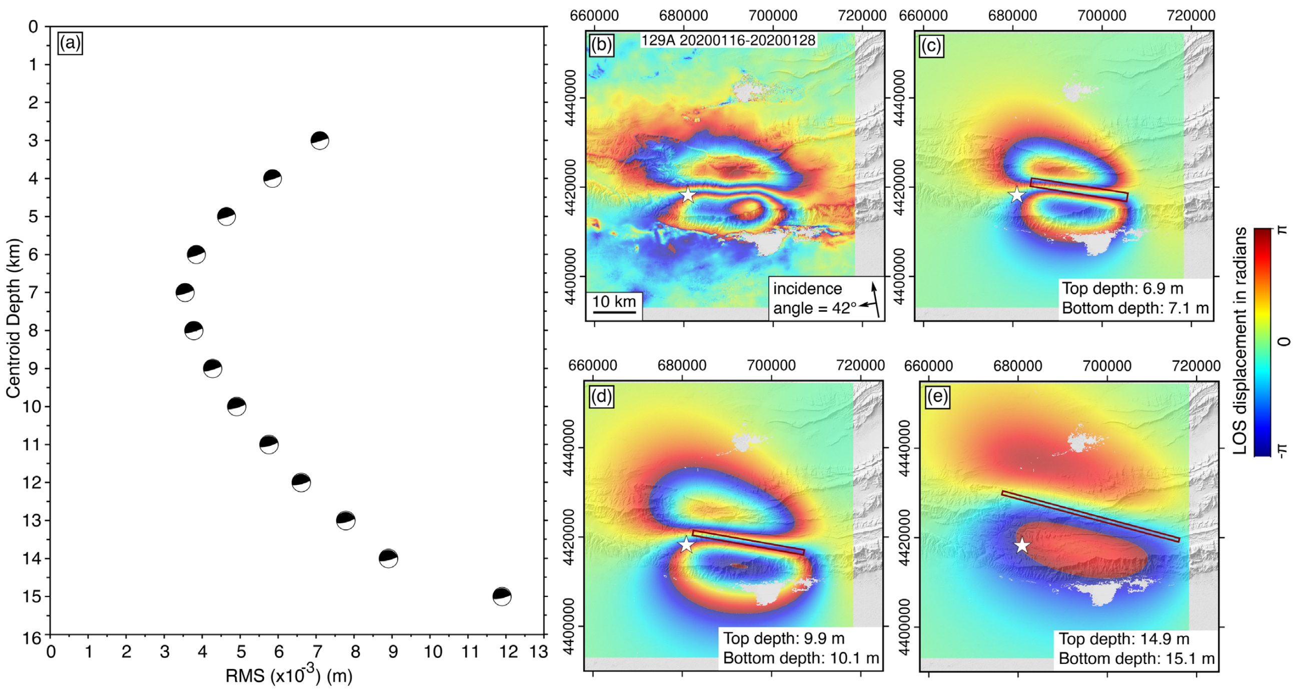


**Figure 3.** (a) Fault centre depth sensitivity tests of our InSAR uniform slip fault models for the 2020 Jiashi main shock. Each focal mechanism shows the minimum-misfit model solution for a fixed centre depth, with all other parameters kept free in each inversion. The *x*-axis is root mean square error (RMS) in metres; the *y*-axis shows 1 km increments of fixed centre depth. (b) Observed ascending track interferogram (same as in Fig. 2a). (c) Preferred uniform slip model interferogram, with its (free) centre depth of 7 km. (d) A forward model interferogram with centre depth fixed to 10 km. The forward model used the same uniform slip parameters as in (c) except for the top and bottom depth and the surface projection coordinates. (e) Same as (d) but with a centroid depth of 15 km. The coordinates are in UTM 43N.

Our InSAR model fault plane is 10° different in strike and 17° different in rake from the N-dipping nodal plane of the USGS body-wave moment tensor, and there are even larger discrepancies in strike and rake with the USGS W-Phase and GCMT solutions (Table 2). However, of the four mechanisms the InSAR model strike is most closely aligned with ~E–W trends in local faulting, geological structure and topography. Furthermore, the shallow-dipping nodal planes of the USGS and GCMT models are poorly constrained by teleseismic data and liable to be affected by a strong trade-off between strike and rake (e.g. Beckers & Lay 1995). Our distributed slip model is 17–26 per cent larger in moment than the three available seismological catalogue solutions.

Four other InSAR-derived fault models are also available for comparison (Table 2). Our model is closest to that of He *et al.* (2021) and to the single fault solution of Yu *et al.* (2020); the three models agree to within 4° in strike and dip, to within 6° in rake, and to within 1 km in centroid depth. Yu *et al.*'s preferred, two-fault model is strongly listric, with slip apportioned between a deep, gentle (2°) décollement and a much steeper (52°) ramp. However, we prefer the single-fault solution, as the two-fault models we tested using different configurations of listric and antilistric faults could not yield smaller misfits. Our model is ~2 km deeper and significantly shorter and narrower than a uniform slip model by Yao *et al.* (2021b). However, they do not provide model or residual interferograms, so there is no easy way to assess the accuracy of their model.

Our relocated main shock hypocentre lies beneath the northern limb of Kepingtag anticline, which is located ~6.6 km NNW from one inferred by Ran *et al.* (2020) using local data. However, our

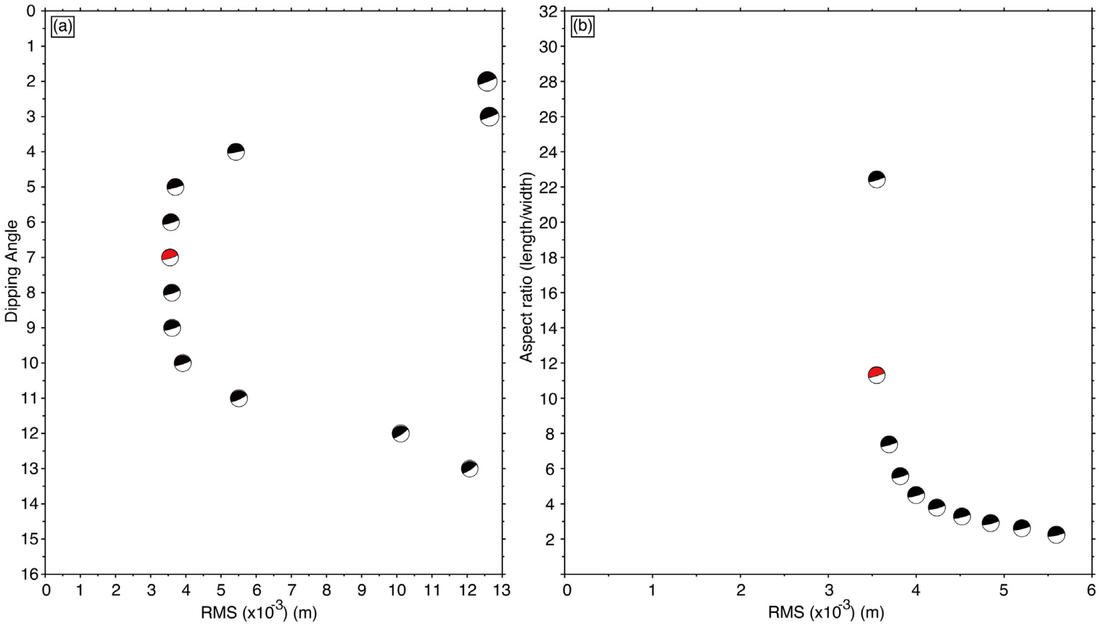


**Figure 4.** (a) Fault dip sensitivity tests of our InSAR uniform slip fault models for the 2020 Jiashi main shock. Each focal mechanism shows the minimum-misfit model solution for a fixed dip angle, with all other parameters kept free in each inversion. The *x*-axis is root mean square error (RMS) in metres; the *y*-axis shows 1° increments of fixed dip. The one with red compression part indicates the optimal uniform slip model. (b) Fault plane width sensitivity tests. Each focal mechanism shows the minimum-misfit model solution for a fixed fault width (obtained by fixing the centroid depth and dip to the minimum misfit values and extending the fault plane up- and downdip at 1 km increments). All other parameters, including slip and fault length, are allowed to vary and the results are plotted according to the aspect ratio of length to width. The red focal mechanism indicates the optimal uniform slip model.

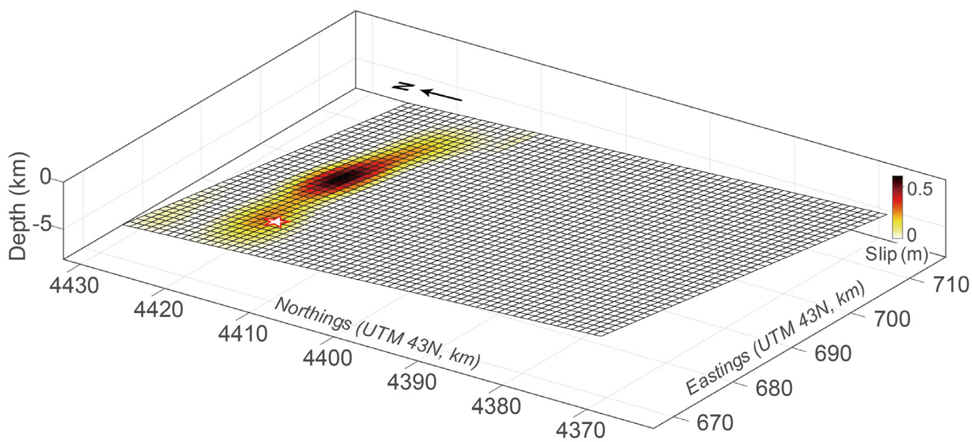


**Figure 5.** The perspective view of the coseismic slip distribution. The fault plane dips to north shallowly. Significant slip occurs over the depth range 6.5–7.4 km. The red star marks the relocated epicentre near the western end of the deformation field for the 2020 Jiashi earthquake.

epicentre is somewhat closer to the InSAR-derived slip distribution patch, lying at its far western end. Both our model and Ran *et al.* (2020)'s show that the Jiashi earthquake is strongly unilateral, rupturing from west to east (Fig. S12). Our relocated epicentre of the 2020 January 17 $m_b$ 4.3 foreshock lies ~3 km SE from the main shock, and the two largest aftershocks ($m_b$ 5.1 and 5.0) lie near the eastern end of the main shock model slip patch (Fig. 1c).

We show the results of our seismological inversions in Fig. 6 and synthetic waveforms for all stations used in the inversion in Figs S10–S11. A probability density function (PDF) of centroid depth results from an inversion with all parameters free shows both the mean and the best-fitting solution at just under 10 km (Fig. 6a). Using teleseismic data offers good constraints on the mechanism only near the centre of the focal sphere, where the pierce-points of teleseismic body waves cluster. As such, the mechanism, and particularly the shallowly dipping nodal plane are poorly constrained (inset mechanism, Fig. 6a). Consequently, we repeated the inversion using double couple nodal planes fixed to match the InSAR-determined fault plane (Fig. 6b). This pushes the PDF slightly deeper, with a mean depth at 11 km, but with a best-fitting solution still at 10 km, and makes only a marginal difference to the overall misfit values. We also show the PDF for the seismologically-determined magnitude in Fig. 6(c), which matches well with the inferred magnitude of the geodetic signal. The model source time function duration of 8–10 s is rather long for a $M_w$ 6.0 thrust earthquake (e.g. Bayasgalan *et al.* 2005; Nissen *et al.* 2007; Elliott *et al.*

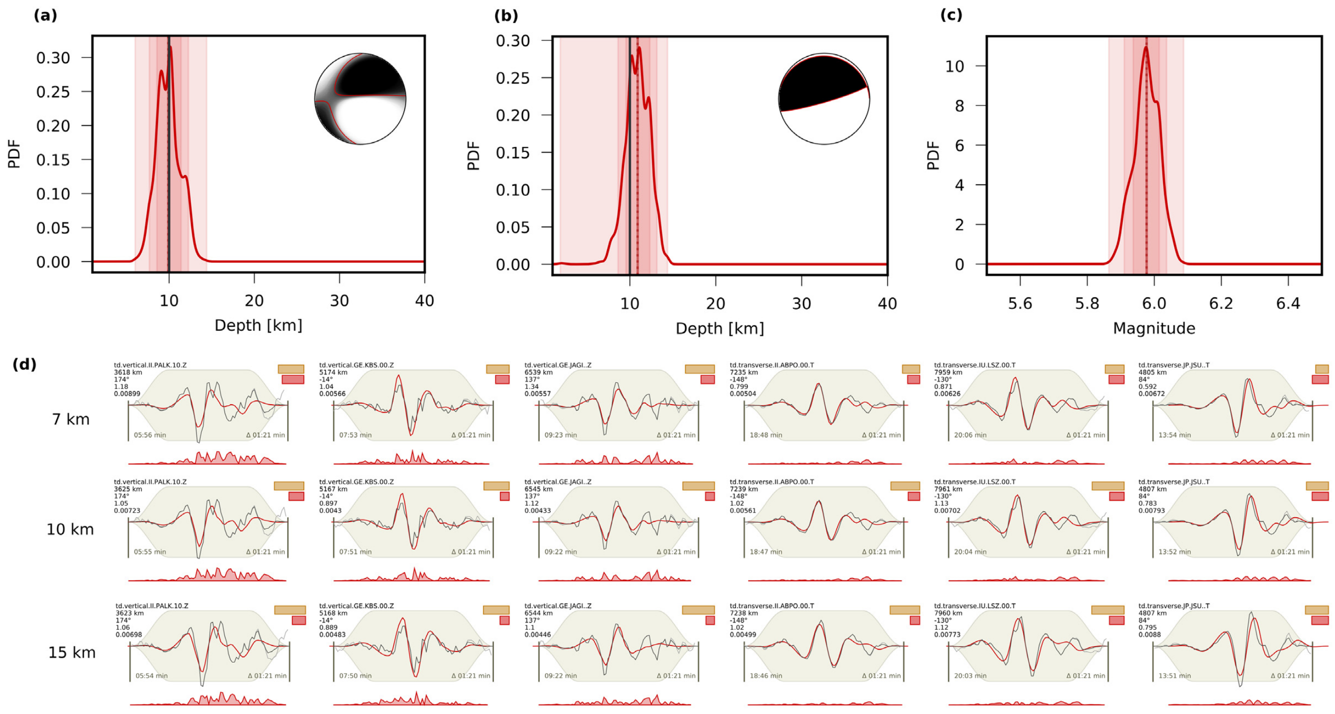


**Figure 6.** Seismological processing results for the 2020 Jiashi main shock. (a) Probability-density function for depth, for an inversion with all parameters free. Inset mechanism shows the mechanism probability density function (greys) and the best-fitting solution (red). (b) Probability–density function for depth, for an inversion with the mechanism constrained to be a double couple matching the InSAR-derived fault plane. (c) Probability–density function for moment, for an inversion with the mechanism constrained to match the InSAR-derived fault plane. (d) Example waveforms for 6 stations (three vertical component, three transverse component). Black traces show the observed data, red line shows the best-fitting inversion result. Text on each waveform indicates the station and component, epicentral distance, and azimuth. Each row of waveforms show synthetics calculated at 7, 10 and 15 km, respectively, as discussed in the text.

2015) and supports our inference of unilateral rupture of a ∼22–37 km fault assuming typical propagation speeds of 1.5–4 km $s^{-1}$ (Chounet *et al.* 2018).

In order to illustrate the constraints that the teleseismic data offer on the centroid depth, we show a set of six example waveforms (three vertical components, three transverse component) and best-fitting synthetics calculated using three fixed centroid depths in Fig. 6(d). The middle row shows waveforms calculated at 10 km centroid depth, which is the best-fitting seismological solution, while the upper row shows waveforms with the depth fixed to match the geodetic results at 7 km, and the lower row shows waveforms with the depth fixed to match the centre of the regionally determine aftershock distribution at 15 km. We discuss these waveform misfits further in the following section.

## 5 DISCUSSION

### 5.1 Depth discrepancy between the 2020 Jiashi main shock and its aftershocks

Our InSAR-derived model suggests that the Jiashi main shock ruptured along the décollement at the base of the sedimentary cover, with a centroid depth of ∼7 km. From the high-quality locally-recorded and double-difference relocated aftershock data, aftershocks cluster along E–W and NNW–SSE trends, with the former matching the ∼40 km length and orientation of our slip model (Figs S12 and S13, Ran *et al.* 2020; Yao *et al.* 2021a; He *et al.* 2021). However, locally recorded aftershocks concentrate at 10–20 km depth, well below the depth of main shock slip resolved by InSAR inversion. We consider two possible explanations for this apparent discrepancy.

The first possible explanation is that the surface deformation captured with InSAR may reflect aseismic afterslip along the décollement, above an earthquake buried within the underlying basement (at the depth of the aftershock concentration) and itself invisible to InSAR. We tested this possibility by forward modelling the interferograms based upon a $M_w$ 6.0 thrust earthquake with the same geometry as our preferred uniform slip model fault but centred at depths of 10 and 15 km, more consistent with the aftershock seismicity (Figs 3c and d). These forward model interferograms match poorly with the observed InSAR data, with notably more far-field deformation and a broader spacing of fringes between the southern and northern lobes. However, the fact that this surface deformation remains distinguishable leads us to rule out the possibility that coseismic slip is too deep to be resolved with InSAR.

The second possible explanation is that the InSAR captures main shock slip but that well-located aftershocks are vertically separated from the main shock within the underlying basement, perhaps concentrated within a lobe of positive Coulomb stress change expected below the base of a thrust or reverse fault (e.g. Lin & Stein 2004; Zhou *et al.* 2019). He *et al.* (2021) showed that double-difference relocated aftershocks concentrate along two steep planes within the basement; they then used Coulomb stress calculations to estimate the kinematics of these faults most consistent with static stress triggering by the shallower main shock. This implies that the basement aftershocks involved N–S-oriented sinistral and steep, S-dipping reverse faulting. However, this does not explain the absence of shallow aftershocks within positive Coulomb stress lobes expected above the top main shock fault edge. This might reflect an effect on the stress field from the stress-free boundary of the Earth's surface, that the faults within the sediments above the décollement may exhibit velocity-strengthening friction, favouring aseismic creep over seismic slip (Karasözen *et al.* 2016), or that the seismic network is insensitive to shallow events due to its average station spacing of ~30 km. Local seismic networks are able to constrain the focal depth most accurately only if *Pg* and *Sg* phases are recorded at epicentral distances of less than ~1–2 times of focal depths and the average station spacing is also less than ~1–2 times of focal depths (Gomberg *et al.* 1990). Therefore, the apparent absence of shallow events may be an artefact, as the stations with average spacing of ~30 km cannot record aftershocks shallower than 15 km depth.

We agree with the explanation favoured by He *et al.* (2021) that the main shock and aftershocks are vertically separated, as our teleseismic waveform inversion reinforces that the geodetically imaged signal is indeed coseismic. The waveform misfit differences between depths of 10 and 7 km are minimal (Fig. 6d). However, synthetics are notably too broad at all six of the stations shown when the depth is increased to 15 km. Due to the cross-correlation based alignment, synthetics are typically aligned on the dominant peak to minimise misfit. However, at 15 km depth, this leads to the peaks to either side being too far out from the main peak due to the increase separation between direct and depth phases. Thus, we conclude that the seismological data are consistent with the deformation signal detected using InSAR, but are notably shallower than the aftershocks located using regional seismology.

Main shock–aftershock depth discrepancies are not uncommon and several other earthquake sequences also exhibit similar characteristics. The 2000 $M_w$ 6.6 Torrori (Japan), 2003 $M_w$ 6.6 Bam (Iran), 2008 $M_w$ 7.9 Wenchuan (China), 2009 $M_w$ 5.9 Karonga (Malawi), 2011 $M_w$ 5.9 Simav (Turkey) and 2014 $M_w$ 6.1 South Napa (California) earthquakes all exhibited shallower main shock slip, resolved mostly using geodesy, with deeper aftershock distributions, resolved using seismology (Semmane *et al.* 2005; Jackson *et al.* 2006; Tong *et al.* 2010; Wei *et al.* 2015; Karasözen *et al.* 2016; Gaherty *et al.* 2019). Similar patterns were also observed in $M_w$ ~6 earthquakes and aftershock sequences at Qeshm (2005) and Fin (2006) in the Zagros Simply Folded Belt, Iran (Nissen *et al.* 2010; Roustaei *et al.* 2010). These are especially analogous to the Jiashi sequence, as the Zagros main shocks were centred within a thick sedimentary cover, with aftershock microseismicity vertically separated within the underlying basement (Nissen *et al.* 2014). Finally, we recollect that the 2003 February 24 $M_w$ 6.2 Jiashi earthquake in the foreland basin south of the Kepingtag was centred at ~5–7 km depth, but exhibited aftershocks at ~15–25 km depth (Huang *et al.* 2006; Sloan *et al.* 2011).

### 5.2 Structural interpretation of the 2020 Jiashi rupture

Coseismic uplift in the 2020 $M_w$ 6.0 Jiashi earthquake resolved by InSAR is centred along the back limb of the Kepingtag anticline (Figs 7a–d). Seismic reflection profiles and balanced geological cross-sections depict this as a fault-propagation fold, with Palaeozoic–Mesozoic sediments thrust over Cenozoic strata along the moderately northward-dipping Kepingtag fault, which branches off a décollement with an estimated depth of ~5–10 km (Yin *et al.* 1998; Allen *et al.* 1999; Yang *et al.* 2002, 2010). Projecting our slip model onto a modified geological cross-section suggests that the 2020 earthquake ruptured the décollement where it intersects with the base of the Kepingtag thrust fault (Fig. 7e).

A striking feature of our distributed slip model is its elongate shape, with a length-to-width aspect ratio of greater than 4 (Fig. 5). This indicates that the earthquake was able to propagate readily along strike, but was prevented from doing so up- and down-dip. We consider two potential causes of this pattern. One possibility is that the stratigraphic configuration could have determined where slip was able to propagate, with rupture restricted to competent rocks such as the lowermost Cambrian limestone. A similar explanation was proposed by Elliott *et al.* (2015) for the elongate slip distribution (length-to-width ratio ~3) of the 2013 $M_w$ 6.2 Khaki-Shonbe earthquake in the Zagros fold-and-thrust belt, where Infracambrian Hormuz evaporites and Cretaceous Kazhdumi mudstones were inferred to have controlled the bottom and top of the rupture, respectively. Length-to-width ratios of ~3–4 inferred for the 2006 Fin and 2019 Khalili earthquakes (both $M_w$ 5.7) suggest that this may be a common feature of Zagros ruptures (Roustaei *et al.* 2010; Jamalreyhani *et al.* 2021). Another possible mechanism could be due to structural complexities in the fault geometry. This was discussed by Elliott *et al.* (2011) for the 2008 and 2009 Qaidam $M_w$ 6.3 earthquakes, whose vertical segregation resulted from disruption of the rupture plane by a cross-cutting, conjugate reverse fault. In the 2020 Jiashi event, we suggest that the abrupt change in dip angle between the subhorizontal décollement and the much steeper Kepingtag fault may have provided a barrier to rupture. Our testing of listric fault geometries is in good agreement with the inference that there was minimal slip on the steeper fault. Although the current data does not allow us to distinguish between the two mechanisms, there is a clear structural or lithological control on the extent of coseismic slip during the main shock.

### 5.3 Regional distribution of seismicity and seismic hazard

The Pamir and Tian Shan jointly accommodate a crustal shortening of 20–25 mm yr$^{-1}$, nearly half of the total India-Eurasia convergence rate (Abdrakhmatov *et al.* 1996; Zubovich *et al.* 2010). The southwestern margin of the Tian Shan is characterized by frequent seismicity, mostly with thrust faulting and strike-slip mechanisms. Here, we use our own calibrated earthquake relocations together with previous waveform modelling studies to assess the finer-scale distribution of seismicity across this region.

From the calibrated earthquake relocations, it is apparent that seismicity is not concentrated along the frontal Kepingtag belt, but is distributed throughout the fold-and-thrust belt as well as the adjacent foreland to the south. The shallow events occur to the north of the frontal Kepingtag anticline as well as in the foreland to the south. This pattern indicates that all stacks of the thrust sheets may be simultaneously capable of generating earthquakes, even as one of them might be most favourable at a particular time due to a variable stress state and the history of previous earthquakes. This inference is also supported by geomorphological and geochronological data (Yang *et al.* 2006) and suggests that seismic hazard is high across the region, rather than being focused along the range front.

Moreover, the seismic hazard in the Kepingtag region is not only restricted to faulting along the décollement but also within the folded cover rocks and the piedmont area. Reliable earthquake centroid and focal depths—from teleseismic or regional waveform modelling (Fan *et al.* 1994; Ghose *et al.* 1998; Sloan *et al.* 2011) and our own calibrated hypocentral relocations—are concentrated at depths shallower than 25 km, except for two isolated events at 29–35 km (Fig. 8). The 1997 Jiashi earthquake swarm and the

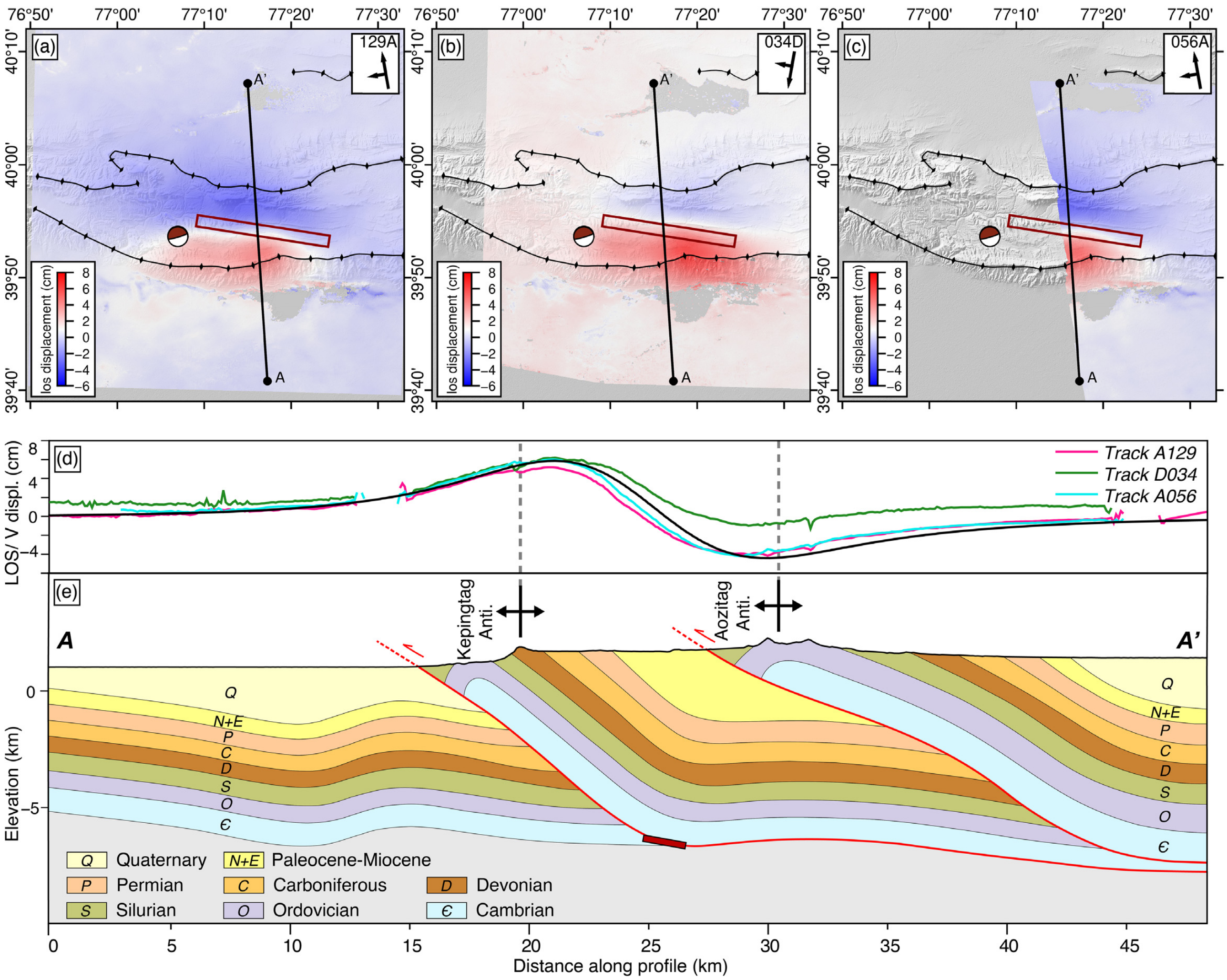


**Figure 7.** Coseismic LOS displacements in the 2020 Jiashi earthquake from unwrapped interferograms on tracks (a) 129A, (b) 034D and (c) 056A. Black lines with ticks show the traces of the Aozitang (north) and Kepingtag (south) fold axes. The dark red rectangle is the uniform slip model fault plane, centred at ∼7 km depth. (d) LOS displacement profiles and vertical displacement profile (track A129 in pink, D034 in green, A056 in cyan and vertical displacement in black) along profile A–A' in (a), (b) and (c). Maximum LOS displacements are ∼7.5 cm towards the satellite and ∼4 cm away from the satellite. Vertical displacement field is predicted by our best fitting, InSAR-derived distributed slip model. (e) Geological cross-section along the profile A–A', interpreted from seismic reflection profiles (Yang *et al.* 2010). The surface topography is extracted from the 30 m resolution SRTM DEM. The dark red rectangle indicates the uniform slip model fault plane.

2003 Bachu-Jiashi sequence all occurred on blind faults in the piedmont area ∼50 km south of the Kepingtag frontal thrust. The largest events between 1997 and 1998 ($M_w$ 5.7, 5.9, 6.0 and 6.3) represented activity on normal faulting or left-lateral strike-slip faulting at mid-crustal depths of ∼12–20 km, while the 2003 events involved much shallower thrust faulting (Sloan *et al.* 2011). Within the Kepingtag fold-and-thrust belt, most of the reliable centroid depths are greater than 10 km, indicating faulting within the basement is below the décollement. Though usually depicted as a 'thin-skinned' fold-and-thrust belt, the Kepingtag basement clearly accommodates shortening by reverse faulting, and should therefore be considered as an important source of seismic hazard.

## 6 CONCLUSION

We use InSAR data to characterize the coseismic surface deformation and model the fault geometry and slip distribution of the 2020 January 19 $M_w$ 6.0 Jiashi earthquake. Modelled coseismic uplift is centred on the back limb of the Kepingtag anticline, consistent with previous structural models that depict this as a fault-propagation fold. Our best-fitting model fault plane dips ∼7° northward at depth of ∼7 km, placing it on or close to the mapped décollement at the base of the folded sedimentary cover. This depth is consistent with teleseismic body-waveforms, confirming that the slip modelled with InSAR occurred coseismically. The small (∼1/4) width to length ratio of our model slip distribution hints at structural and/or lithological controls on slip propagation; for example, rupture may have been prevented from advancing up-dip by the abrupt change of dip angle between the subhorizontal décollement and the much steeper Kepingtag thrust. Published seismological studies show that aftershocks cluster within underlying basement rocks at ∼10–20 km depth, vertically separated from the main shock slip. Our own relocated background seismicity also shows a prevalence of seismicity at basement depths throughout the Kepingtag belt and its foreland, hinting at rheological controls on the depths at which earthquakes occur.

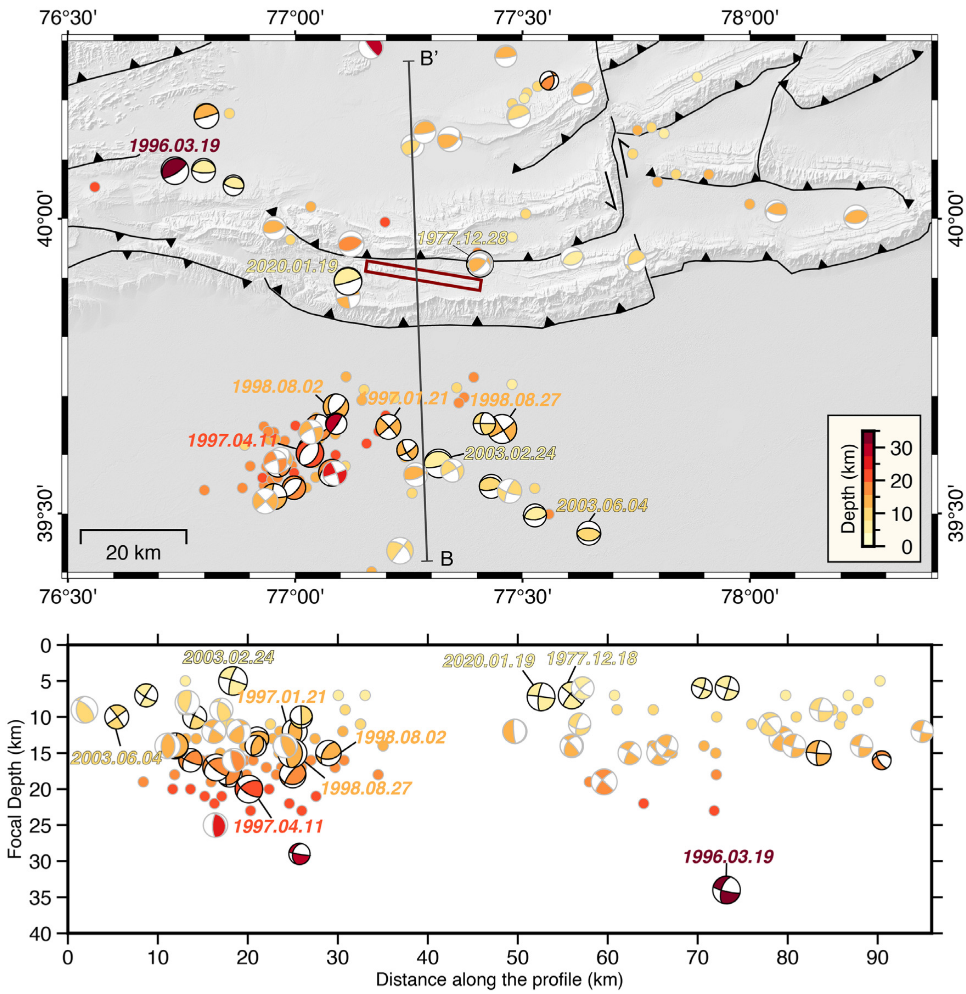


**Figure 8.** Calibrated relocated earthquakes from 1977 to 2020 in the Jiashi area, coloured according to the best available estimate of depth. Focal mechanisms determined by teleseismic and regional waveform modelling, including some from the GCMT catalogue. The depths of focal mechanisms with black outlines are determined by teleseismic and regional waveform modelling and depth phases, while those with grey outlines are our own calibrated focal depths (see Table 2 for full details). Other moderate relocated earthquakes without focal mechanisms are shown as dots.

## ACKNOWLEDGMENTS

SW was supported by the China Scholarship Council and a Graduate Award from University of Victoria. EN and RJ were funded separately by the Natural Science and Engineering Research Council of Canada (⟨0:funding-source 3:href="http://dx.doi.org/10.13039/501100000038"⟩NSERC⟨/0:funding-source⟩), the Canada Foundation for Innovation (CFI) and the BC Knowledge Develoment Fund (BCKDF). EN also acknowledges support from a Canada Research Chair. TC was supported by the Royal Society (UK) under URF\R1\180088. TC was also supported through COMET, the UK Natural Environment Research Council's Centre for the Observation and Modelling of Earthquakes, Volcanoes, and Tectonics. We are grateful to two anonymous reviewers for their constructive comments which significantly improve the manuscript.

## DATA AVAILABILITY

Interferograms were constructed using Copernicus Sentinel-1 data (2020) available from https://scihub.copernicus.eu/, and processed in GAMMA software (https://www.gamma-rs.ch/). InSAR modelling codes are available from EN upon request. Earthquakes were relocated using *Mloc* software (https://seismo.com/mloc/), using starting location parameters from the International Seismological Centre Bulletin (Centre International Seismological 2021). Full calibrated relocation results will be posted to the USGS ScienceBase website for the Global Catalog of Calibrated Earthquake Locations (GCCEL) (Benz 2021). We also used focal mechanism data from the Global Centroid Moment Tensor project (Dziewonski 1981). Several of the figures in the paper were plotted using Generic Mapping Tools (Wessel *et al.* 2019).

## REFERENCES

Abdrakhmatov, K.Y. *et al.*, 1996. Relatively recent construction of the Tien Shan inferred from GPS measurements of present-day crustal deformation rates, *Nature,* **384**(6608), 450–453.

Ainscoe, E.A., Elliott, J.R., Copley, A., Craig, T.J., Li, T., Parsons, B.E. & Walker, R.T., 2017. Blind thrusting, surface folding, and the development of geological structure in the Mw 6.3 2015 Pishan (China) earthquake, *J. geophys. Res.,* **122**(11), 9359–9382.

Allen, M.B., Vincent, S.J. & Wheeler, P.J., 1999. Late Cenozoic tectonics of the Kepingtage thrust zone: interactions of the Tien Shan and Tarim Basin, northwest China, *Tectonics,* **18**(4), 639–654.

Avouac, J.P. & Tapponnier, P., 1993. Kinematic model of active deformation in central Asia, *Geophys. Res. Lett.,* **20**(10), 895–898.

Bayasgalan, A., Jackson, J. & McKenzie, D., 2005. Lithosphere rheology and active tectonics in Mongolia: relations between earthquake source parameters, gravity and gps measurements, *J. geophys. Int.,* **163**(3), 1151–1179.

Beckers, J. & Lay, T., 1995. Very broadband seismic analysis of the 1992 Flores, Indonesia, earthquake ($M_w$ = 7.9), *J. geophys. Res.,* **100**(B9), 18179–18193.

Benz, H.M., 2021. Global Catalog of Calibrated Earthquake Locations, *U.S. Geological Survey data release*.https://www.sciencebase.gov/catalog/item/59fb91fde4b0531197b16ac7

Bie, L., Ryder, I., Nippress, S. E.J. & Bürgmann, R., 2014. Coseismic and post-seismic activity associated with the 2008 $M_w$ 6.3 Damxung earthquake, Tibet, constrained by InSAR, *J. geophys. Int.,* **196**(2), 788–803.

Bro, R. & De Jong, S., 1997. A fast non-negativity-constrained least squares algorithm, *J. Chemometr.,* **11**(5), 393–401.

Burchfiel, B.C. *et al.*, 1999. Crustal shortening on the margins of the Tien Shan, Xinjiang, China, *Int. Geol. Rev.,* **41**(8), 665–700.

Centre International Seismological, https://doi.org/10.31905/D808B830, . ,

Chen, J., Ran, Y., Yang, X. & Xu, X., 2006. Character of Late Quaternary activity of the east segment of the front-edge faults of Kalpintag, *Seismol. Geol.,* **28**(2), 258–268 (in Chinese with English abstract).

Chounet, A., Vallée, M., Causse, M. & Courboulex, F., 2018. Global catalog of earthquake rupture velocities shows anticorrelation between stress drop and rupture velocity, *Tectonophysics,* **733,** 148–158.

Copley, A., 2014. Postseismic afterslip 30 years after the 1978 Tabas-e-Golshan (Iran) earthquake: observations and implications for the geological evolution of thrust belts, *J. geophys. Int.,* **197**(2), 665–679.

Copley, A., Karasozen, E., Oveisi, B., Elliott, J.R., Samsonov, S. & Nissen, E., 2015. Seismogenic faulting of the sedimentary sequence and laterally variable material properties in the Zagros Mountains (Iran) revealed by the August 2014 Murmuri (E. Dehloran) earthquake sequence, *J. geophys. Int.,* **203**(2), 1436–1459.

Davis, T.L., Namson, J. & Yerkes, R.F., 1989. A cross section of the Los Angeles area: seismically active fold and thrust belt, the 1987 Whittier Narrows earthquake, and earthquake hazard, *J. geophys. Res.,* **94**(B7), 9644–9664.

Dziewonski (1981) Journal of Geophysical Research: Solid Earth *2825,*, 01480227

Elliott, J.R. *et al.*, 2015. The 2013 Mw 6.2 Khaki-Shonbe (Iran) Earthquake: insights into seismic and aseismic shortening of the Zagros sedimentary cover, *Earth Space Sci.,* **2**(11), 435–471.

Elliott, J.R., Copley, A.C., Holley, R., Scharer, K. & Parsons, B., 2013. The 2011 Mw 7.1 Van (Eastern Turkey) earthquake, *J. geophys. Res.,* **118**(4), 1619–1637.

Elliott, J.R., Parsons, B., Jackson, J.A., Shan, X., Sloan, R.A. & Walker, R.T., 2011. Depth segmentation of the seismogenic continental crust: the 2008 and 2009 Qaidam earthquakes, *Geophys. Res. Lett.,* **38**(6), 1–6.

Elliott, J.R., Walters, R.J. & Wright, T.J., 2016. The role of space-based observation in understanding and responding to active tectonics and earthquakes, *Nat. Commun.,* **7,** doi:10.1038/ncomms13844.

Engdahl, R.E., Jackson, J.A., Myers, S.C., Bergman, E.A. & Priestley, K., 2006. Relocation and assessment of seismicity in the Iran region, *J. geophys. Int.,* **167**(2), 761–778.

Fan, G., Ni, J.F. & Wallace, T.C., 1994. Active tectonics of the Pamirs and Karakorum, *J. geophys. Res.,* **99**(B4), 7131 , doi:10.1029/93JB02970.

Funning, G.J., Parsons, B., Wright, T.J., Jackson, J.A. & Fielding, E.J., 2005. Surface displacements and source parameters of the 2003 Bam (Iran) earthquake from Envisat advanced synthetic aperture radar imagery, *J. geophys. Res.,* **110**(B9), doi:10.1029/2004JB003338.

Gaherty, J.B. *et al.*, 2019. Faulting processes during early-stage rifting: seismic and geodetic analysis of the 2009-2010 Northern Malawi earthquake sequence, *J. geophys. Int.,* **217**(3), 1767–1782.

Gao, R. *et al.*, 2013. Fine crustal structure beneath the junction of the southwest Tian Shan and Tarim Basin, NW China, *Lithoshere,* **5**(4), 382–392.

Gaudreau, É., Nissen, E., Bergman, E.A., Benz, H.M., Tan, F. & Karasözen, E., 2019. The August 2018 Kaktovik earthquakes: active tectonics in northeastern Alaska revealed with InSAR and seismology, *Geophys. Res. Lett.,* **46**(24), 14 412–14 420.

Ghose, S., Hamburger, M.W. & Ammon, C.J., 1998. Source parameters of moderate-sized earthquakes in the Tien Shan, central Asia from regional moment tensor inversion, *Geophys. Res. Lett.,* **25**(16), 3181–3184.

Goldstein, R.M., Zebker, H.A. & Werner, C.L., 1988. Satellite radar interferometry: two-dimensional phase unwrapping, *Radio Sci.,* **23**(4), 713–720.

Gomberg, J.S., Shedlock, K.M. & Roecker, S.W., 1990. The effect of S-wave arrival times on the accuracy of hypocenter estimation, *Bull. seism. Soc. Am.,* **80**(6A), 1605–1628.

He, Y., Wang, T., Fang, L. & Zhao, L., 2021. The 2020 Mw 6.0 Jiashi earthquake: coinvolvement of thin-skinned thrusting and basement shortening in shaping the Keping-Tage fold-and-thrust belt in Southwestern Tian Shan, *Seismol. Res. Lett.,* **93**(2A), 680–692.

Heimann, S. *et al.*, 2018. Grond: a probabilistic earthquake source inversion framework. V. 1.0. GFZ Data Services. https://doi.org/10.5880/GFZ.2.1.2018.003.

Hendrix, M.S., Graham, S.A., Carroll, A.R., Sobel, E.R., McKnight, C.L., Schulein, B.J. & Wang, Z., 1992. Sedimentary record and climatic implications of recurrent deformation in the Tian Shan: evidence from Mesozoic strata of the north Tarim, south Junggar, and Turpan basins, northwest China, *Bull. geol. Soc. Am.,* **104**(1), 53–79.

Huang, Y., Yang, J.S. & Zhang, T.Z., 2006. Relocation of the Bachu-Jiashi, Xinjiang earthquake sequence in 2003 using the double-difference location algorithm, *Acta Geophys. Sin.,* **49**(1), 162–169.

Jackson, J. *et al.*, 2006. Seismotectonic, rupture process, and earthquake-hazard aspects of the 2003 December 26 Bam, Iran, earthquake, *J. geophys. Int.,* **166**(3), 1270–1292.

Jamalreyhani, M. *et al.*, 2021. The 2019-2020 Khalili (Iran) earthquake sequence—anthropogenic seismicity in the Zagros simply folded belt?, *J. geophys. Res.,* **126**(12), e22797 , doi:10.1029/2021JB022797.

Jones, L. *et al.*, 1994. The magnitude 6.7 Northridge, California, earthquake of 17 January 1994, *Science,* **266**(5184), 389–397.

Jónsson, S., Zebker, H., Segall, P. & Amelung, F., 2002. Fault slip distribution of the 1999 Mw 7.1 Hector Mine, California, earthquake, estimated from satellite radar and GPS measurements, *Bull. seism. Soc. Am.,* **92**(4), 1377–1389.

Jordan, T.H. & Sverdrup, K.A., 1981. Teleseismic location techniques and their application to earthquake clusters in the South-Central Pacific, *Bull. seism. Soc. Am.,* **71,** 1105–1130.

Karasözen, E. *et al.*, 2018. The 2017 July 20 $M_w$ 6.6 Bodrum-Kos earthquake illuminates active faulting in the Gulf of Gökova, SW Turkey, *J. geophys. Int.,* **214**(1), 185–199.

Karasözen, E., Nissen, E., Bergman, E.A. & Ghods, A., 2019. Seismotectonics of the Zagros (Iran) From Orogen-Wide, Calibrated Earthquake Relocations, *J. geophys. Res.,* **124**(8), 9109–9129.

Karasözen, E., Nissen, E., Bergman, E.A., Johnson, K.L. & Walters, R.J., 2016. Normal faulting in the Simav graben of western Turkey reassessed with calibrated earthquake relocations, *J. geophys. Res.,* **121**(6), 4553–4574.

Kennett, B.L.N., Engdahl, E.R. & Buland, R., 1995. Constraints on seismic velocities in the Earth from traveltimes, *J. geophys. Int.,* **122**(1), 108–124.

Kulikova, G. & Krüger, F., 2017. Historical seismogram reproductions for the source parameters determination of the 1902, Atushi (Kashgar) earthquake, *J. Seismol.,* **21**(6), 1577–1597.

Li, S. & Barnhart, W.D., 2020. Impacts of topographic relief and crustal heterogeneity on coseismic deformation and inversions for fault geometry and slip: a case study of the 2015 Gorkha earthquake in the Central Himalayan Arc, *Geochem. Geophys. Geosyst.,* **21**(12), e09413 , doi:10.1029/2020GC009413.

Lin, J. & Stein, R.S., 2004. Stress triggering in thrust and subduction earthquakes and stress interaction between the southern San Andreas and nearby thrust and strike-slip faults, *J. geophys. Res.,* **109**(B2), doi:10.1029/2003JB002607.

Mallick, R., Bürgmann, R., Johnson, K. & Hubbard, J., 2021. A unified framework for earthquake sequences and the growth of geological structure in fold-thrust belts, *J. geophys. Res.,* **126**(9), doi:10.1029/2021JB022045.

Nishidai, T. & Berry, J.L., 1990. Structure and hydrocarbon potential of the Tarim Basin (Nw China) from satellite imagery, *J. Petrol. Geol.,* **13**(1), 35–58.

Nissen, E., Ghorashi, M., Jackson, J., Parsons, B. & Talebian, M., 2007. The 2005 Qeshm Island earthquake (Iran) - a link between buried reverse faulting and surface folding in the Zagros Simply Folded Belt?, *J. geophys. Int.,* **171**(1), 326–338.

Nissen, E., Jackson, J., Jahani, S. & Tatar, M., 2014. Zagros "phantom earthquakes" reassessed - the interplay of seismicity and deep salt flow in the Simply Folded Belt?, *J. geophys. Res.,* **119**(4), 3561–3583.

Nissen, E., Tatar, M., Jackson, J.A. & Allen, M.B., 2011. New views on earthquake faulting in the Zagros fold-and-thrust belt of Iran, *J. geophys. Int.,* **186**(3), 928–944.

Nissen, E., Yamini-Fard, F., Tatar, M., Gholamzadeh, A., Bergman, E., Elliott, J.R., Jackson, J.A. & Parsons, B., 2010. The vertical separation of main shock rupture and microseismicity at Qeshm island in the Zagros fold-and-thrust belt, Iran, *Earth planet. Sci. Lett.,* **296**(3–4), 181–194.

Okada, Y., 1985. Surface deformation due to shear and tensile faults in a half-space, *Bull. seism. Soc. Am.,* **75**(4), 1135–1154.

Pousse-Beltran, L., Nissen, E., Bergman, E.A., Cambaz, M.D., Gaudreau, É., Karasözen, E. & Tan, F., 2020. The 2020 $M_w$ 6.8 Elazığ (Turkey) earthquake reveals rupture behavior of the East Anatolian Fault, *Geophys. Res. Lett.,* **47**(13), e88136 , doi:10.1029/2020GL088136.

Press, W.H., Flannery, B.P., Teukolsky, S.A. & Vetterling, W.T., 1992. *Numerical Recipes in C: The Art of Scientific Computing,* 2nd edn, Cambridge Univ. Press.

Ran, H., Shangguan, W. & Liu, D., 2020. Location study of Xinjiang Jiashi Ms6.4 earthquake and aftershocks sequence on January 19th, 2020, *Inland Earthq.,* **34(1),** 56–61.

Ran, Y., Yang, X., Xu, X., Cheng, J. & Chen, L., 2006. Deformation pattern and shortening rates in the east part of Kalpin Thrust system in southwest Tianshan during late Quaternary, *Seismol. Geol.,* **28**(2), 179–193.

Reigber, C. *et al.*, 2001. New space geodetic constraints on the distribution of deformation in Central Asia, *Earth planet. Sci. Lett.,* **191**(1–2), 157–165.

Roustaei, M. *et al.*, 2010. The 2006 March 25 Fin earthquakes (Iran)-insights into the vertical extents of faulting in the Zagros Simply Folded Belt, *J. geophys. Int.,* **181**(3), 1275–1291.

Semmane, F., Cotton, F. & Campillo, M., 2005. The 2000 Tottori earthquake: a shallow earthquake with no surface rupture and slip properties controlled by depth, *J. geophys. Res.,* **110**(3), 1–13.

Sloan, R.A., Jackson, J.A., Mckenzie, D. & Priestley, K., 2011. Earthquake depth distributions in central Asia, and their relations with lithosphere thickness, shortening and extension, *J. geophys. Int.,* **185**(1), 1–29.

Tong, X., Sandwell, D.T. & Fialko, Y., 2010. Coseismic slip model of the 2008 Wenchuan earthquake derived from joint inversion of interferometric synthetic aperture radar, GPS, and field data, *J. geophys. Res.,* **115**(B4), 1–19.

Walker, R., Jackson, J. & Baker, C., 2003. Surface expression of thrust faulting in eastern Iran: source parameters and surface deformation of the 1978 Tabas and 1968 Ferdows earthquake sequences, *J. geophys. Int.,* **152**(3), 749–765.

Walker, R.T., Bergman, E.A., Szeliga, W. & Fielding, E.J., 2011. Insights into the 1968-1997 Dasht-e-Bayaz and Zirkuh earthquake sequences, eastern Iran, from calibrated relocations, InSAR and high-resolution satellite imagery, *J. geophys. Int.,* **187**(3), 1577–1603.

Wang, D., Zhao, B., Yu, J. & Tan, K., 2020. Active tectonic deformation around the Tarim Basin inferred from dense GPS measurements, *Geod. Geodyn.,* **11**(6), 418–425.

Wei, S., Barbot, S., Graves, R., Lienkaemper, J.J., Wang, T., Hudnut, K., Fu, Y. & Helmberger, D., 2015. The 2014 Mw 6.1 South Napa earthquake: a unilateral rupture with shallow asperity and rapid afterslip, *Seismol. Res. Lett.,* **86**(2A), 344–354.

Werner, C., Wegmüller, U., Strozzi, T. & Wiesmann, A., 2000. Gamma SAR and interferometric processing software, in *Proceedings of the ERS-ENVISAT Symposium,* Gothenburg, Sweden.

Wessel, P., Luis, J., Uieda, L., Scharroo, R., Wobbe, F., Smith, W. & Tian, D., 2019. The generic mapping tools version 6, *Geochem. Geophys. Geosyst.,* **20**(11), 5556–5564.

Weston, J., Ferreira, A.M.G. & Funning, G.J., 2011. Global compilation of interferometric synthetic aperture radar earthquake source models: 1. Comparisons with seismic catalogs, *J. geophys. Res.,* **116**(B8), B08408 , doi:10.1029/2010JB008131.

Wimpenny, S. & Scott Watson, C., 2020. gWFM: a global catalog of moderate-magnitude earthquakes studied using teleseismic body waves, *Seismol. Res. Lett.,* **92**(1), 212–226.

Windley, B.F., Allen, M.B., Zhang, C., Zhao, Z.Y. & Wang, G.R., 1990. Paleozoic accretion and Cenozoic redeformation of the Chinese Tien Shan Range, central Asia, *Geology,* **18**(2), 128–131.

Wright, T.J., Lu, Z. & Wicks, C., 2004. Constraining the slip distribution and fault geometry of the Mw 7.9, 3 November 2002, Denali fault earthquake with Interferometric Synthetic Aperture Radar and Global Positioning System data, *Bull. seism. Soc. Am.,* **94**(6 Suppl. B), 175–189.

Wright, T.J., Parsons, B.E., Jackson, J.A., Haynes, M., Fielding, E.J., England, P.C. & Clarke, P.J., 1999. Source parameters of the 1 October 1995 Dinar (Turkey) earthquake from SAR interferometry and seismic bodywave modelling, *Earth planet. Sci. Lett.,* **172**(1–2), 23–37.

Xinjiang Bureau of Geology and Mineral Resources, 1993. *Regional Geology of Xinjiang Uygur Autonomous Region,* Geological Publishing House.

Xu, Y., Roecker, S.W., Wei, R., Zhang, W. & Wei, B., 2006. Analysis of seismic activity in the crust from earthquake relocation in the central Tien Shan, *Bull. seism. Soc. Am.,* **96**(2), 737–744.

Yang, H. *et al.*, 2010. Tectonic characteristics of the Late Cenozoic south Tianshan fold-and-thrust belt, *Quater. Sci.,* **30**(5), 1030–1043 (in Chinese with English abstract).

Yang, X., Ran, Y., Song, F., Xu, X., Cheng, J., Min, W., Han, Z. & Chen, L., 2006. The analysis for crust shortening of Kalpin Thrust tectonic zone, south-western Tianshan, Xinjiang, China, *Seismol. Geol.,* **28**(2), 194–204.

Yang, Z.X., Zhao, J.R., Zhang, X.K., Zhang, C.K., Cheng, S.X., Duan, Y.L., Zhang, J.S. & Wang, S.J., 2002. Tomographic determination of the upper crustal structure in the Jiashi strong earthquake swarm region, *Acta Seismol. Sin. English Edition,* **15**(2), 162–170.

Yao, Q. *et al.*, 2021a. The 2020 M6.4 Jiashi earthquake: an event that occurred under the décollement on the Kaping Fold-and-Thrust Belt in the Southwestern Tien Shan Mountains, China, *Front. Earth Sci.,* **9**(May), 1–14.

Yao, Y., Wen, S., Li, T. & Wang, C., 2021b. The 2020 Mw6.0 Jiashi earthquake: a fold earthquake event in the southern Tian Shan, northwest China, *Seismol. Res. Lett.,* **92**(2), 859–869.

Yin, A., Craig, P., Harrison, T.M., Ryerson, F.J., Qian, X. & Yang, G., 1998. Late Cenozoic tectonic evolution of the southern Chinese Tian Shan, *Tectonics,* **17**(1), 1–27.

Yu, P., Qiao, X., Xiong, W., Chen, W., Nie, Z., Wang, D., Jia, Z. & Li, J., 2020. Source model for the M w 6.0 earthquake in Jiashi, China on 19 January 2020 from Sentinel-1A InSAR data, *Earth, Planets Space,* **72**(1) , doi:10.1186/s40623-020-01300-4.

Zhang, G., Zhu, L., Song, X., Li, Z., Yang, M., Su, N. & Chen, X., 1999. Predictions of the 1997 strong earthquakes in Jiashi, Xinjiang, China, *Bull. seism. Soc. Am.,* **89**(5), 1171–1183.

Zhang, Z.Q., Chen, J. Y.S. & Lin, J., 2008. Stress interactions between normal faults and adjacent strike-slip faults of 1997 Jiashi earthquake swarm, *Sci. China, D: Earth Sci.,* **51**(3), 431–440.

Zhou, S.Y. & Xu, Z.H., 2000. Fracture characteristics of the 1997 Jiashi, Xinjiang, China, earthquake swarm inferred from source spectra, *Acta Seismol. Sin. English Edition,* **13**(2), 125–135.

Zhou, Z., Kusky, T.M. & Tang, C.-C., 2019. Coulomb stress change pattern and aftershock distributions associated with a blind low-angle megathrust fault, Nepalese Himalaya, *Tectonophysics,* **767,** doi:10.1016/j.tecto.2019.228161.

Zubovich, A.V. *et al.*, 2010. GPS velocity field for the Tien Shan and surrounding regions, *Tectonics,* **29**(6), 1–23.

## SUPPORTING INFORMATION

Supplementary data are available at *GJI* online.

**Figure S1**. Histogram of focal depths from our calibrated relocation.

**Figure S2**. Stations, earthquakes, and ray paths used to determine the relocation cluster hypocentroid.
**Figure S3**. The residual of each arrival in the distance range used for estimating the hypocentroid.
**Figure S4**. Observed phase arrivals and theoretical travel times for epicentral distances of up to 4°.
**Figure S5**. Observed shear phase arrivals and theoretical travel times for epicentral distances of up to 15°.
**Figure S6**. Observed phase arrivals and theoretical travel times for epicentral distances of up to 30°.
**Figure S7**. Station distributions used in teleseismic body waveform inversion.
**Figure S8**. Scatter plots of main shock centroid locations and depths inferred from teleseismic waveform inversion.
**Figure S9**. Scatter plots of other main shock source parameters inferred from teleseismic body waveform inversion.
**Figure S10**. Vertical component of waveform misfits for optimum global solution for the Jiashi main shock.
**Figure S11**. Transverse component of waveform misfits for optimum global solution for the Jiashi main shock.
**Figure S12**. Relocated hypocentres of the 2020 Jiashi sequence from Ran *et al*. (2020).
**Figure S13**. Relocated hypocentres of the 2020 Jiashi sequence from Yao *et al*. (2021b).
**Table S1**. Slip sensitivity tests of the InSAR uniform slip fault model for the 2020 Jiashi main shock.
**Table S2**. The 1-D velocity structure used in our calibrated earthquake relocation.
**Table S3**. Our preferred InSAR distributed slip model.
**Table S4**. Earthquake relocation results from Ran *et al*. (2020).
**Table S5**. Relocated hypocentres and their uncertainties.
**Table S6**. GNSS stations within ∼100 km of the Jiashi epicentre, and coseismic displacements predicted at these sites by our best fitting, InSAR-derived distributed slip model. $V_{e\_\mathrm{GNSS}}$ and $V_{n\_\mathrm{GNSS}}$ are interseismic velocities from Wang et al. (2020).

Please note: Oxford University Press is not responsible for the content or functionality of any supporting materials supplied by the authors. Any queries (other than missing material) should be directed to the corresponding author for the paper.